

CLOUDS AND CHEMISTRY IN THE ATMOSPHERE OF EXTRASOLAR PLANET HR8799 b

TRAVIS S. BARMAN

Lowell Observatory, 1400 W. Mars Hill Rd., Flagstaff, AZ 86001, USA
Email: barman@lowell.edu

BRUCE MACINTOSH, QUINN M. KONOPACKY

Lawrence Livermore National Laboratory, 7000 East Avenue, Livermore, CA 94550, USA

CHRISTIAN MAROIS

National Research Council Canada, Herzberg Institute of Astrophysics, 5071 West Saanich Road, Victoria, BC V9E 2E7, Canada
Draft version March 22, 2011

ABSTRACT

Using the integral field spectrograph OSIRIS, on the Keck II telescope, broad near-infrared H and K -band spectra of the young exoplanet HR8799b have been obtained. In addition, six new narrow-band photometric measurements have been taken across the H and K bands. These data are combined with previously published photometry for an analysis of the planet's atmospheric properties. Thick photospheric dust cloud opacity is invoked to explain the planet's red near-IR colors and relatively smooth near-IR spectrum. Strong water absorption is detected, indicating a Hydrogen-rich atmosphere. Only weak CH_4 absorption is detected at K band, indicating efficient vertical mixing and a disequilibrium CO/CH_4 ratio at photospheric depths. The H -band spectrum has a distinct triangular shape consistent with low surface gravity. New giant planet atmosphere models are compared to these data with best fitting bulk parameters, $T_{\text{eff}} = 1100\text{K} \pm 100$ and $\log(g) = 3.5 \pm 0.5$ (for solar composition). Given the observed luminosity ($\log L_{\text{obs}}/L_{\odot} \sim -5.1$), these values correspond to a radius of $0.75 R_{\text{Jup}}^{+0.17}_{-0.12}$ and mass $\sim 0.72 M_{\text{Jup}}^{+2.6}_{-0.6}$ – strikingly inconsistent with interior/evolution models. Enhanced metallicity (up to $\sim 10 \times$ that of the Sun) along with thick clouds and non-equilibrium chemistry are likely required to reproduce the complete ensemble of spectroscopic and photometric data *and* the low effective temperatures ($< 1000\text{K}$) required by the evolution models.

Subject headings: planetary systems - stars: atmospheres - stars: low-mass, brown dwarfs

1. INTRODUCTION

Direct imaging of exoplanets is now becoming a regular occurrence with the recent discoveries of 2M1207b (Chauvin et al. 2005), Fomalhaut b (Kalas et al. 2008), Beta Pic b (Lagrange et al. 2009), 1RXS J1609 b (Lafrenière et al. 2008), and the quadruple-planetary system HR8799 b, c, d, and e (Marois et al. 2008, 2010). HR8799 is, at present, a rare find among exoplanets with its four potentially massive planets ($\sim 5 - 10 M_{\text{Jup}}$) orbiting a ~ 30 Myr A5 star (Zuckerman et al. 2011), and is the first and, so far, only multi-planet system to be directly imaged. All four planets are accessible to photometric and spectroscopic followup observations across many wavelengths and, in this paper, near-IR spectra of HR8799b are folded into a large set of photometric data for a broad-band analysis of the planet's photospheric properties.

Since its discovery, a number of new photometric and astrometric measurements of the HR8799 system have been made. These new data have broadened the photometric wavelength coverage and extended the time coverage of orbital motion (Metchev et al. 2009; Lafrenière et al. 2009; Hinz et al. 2010; Currie et al. 2011). The very precise astrometric data have already inspired a number of papers focused on the orbital dynamics and formation of the system; however, the conclusions about the planetary masses and long term stability of the system from these works are mixed (Fabrycky & Murray-Clay 2010;

Reidemeister et al. 2009; Goździewski & Migaszewski 2009; Dodson-Robinson et al. 2009). As this paper focuses on photospheric properties, the dynamical nature of the system will not be discussed here.

The goal of this paper is to characterize the properties of HR8799b, independent of what interior/evolution models predict and independent of what the age or dynamics of the system suggest. Following a description of the new spectra and photometry added by this work (Section 2), the available set of photometric and spectroscopic data are compared to similar data for brown dwarfs – the closest analogues to young giant planets (Section 3). The atmospheric cloud and chemical properties of HR8799b are inferred by comparing a new set of substellar atmosphere models to the available set of photometry and spectroscopy (Sections 4 and 5). The results are compared to the predictions of interior/evolution models. Also, given the potential for similarities, a comparison is made between HR8799b and 2M1207b (Section 6). The conclusions from this work are summarized in the last section.

2. OBSERVATIONS AND DATA REDUCTION

2.1. OSIRIS Spectroscopy

Observations of HR8799b were made on July 22, 23, and 30 (UT) of 2009 and on July 11 and 13 (UT) of 2010 at the W. M. Keck Observatory. Natural guide star adaptive optics and the OH-Suppressing Infra-Red Imaging

TABLE 1. OSIRIS OBSERVATIONS

target	#exp	exp. time (s)	band pass	UT date
HR8799b	9	900	<i>K</i>	07-22-09
HD210501	5	30		
BD+14 4774	4	30		
HR8799b	6	900	<i>H</i>	07-23-09
HD 210501	7	30		
BD+14 4774	5	30		
HR8799b	7	900	<i>H</i>	07-30-09
BD+14 4774	7	30		
HR8799b	9	900	<i>K</i>	07-11-10
HD210501	3	30		
HR8799b	8	900	<i>H</i>	07-13-10
HD210501	3	30		

Spectrograph (OSIRIS) instrument (Larkin et al. 2006) were used on the Keck II telescope. Broad-band *H* and *K* spectra were obtained over a $0.32 \times 1.28''$ patch of the sky surrounding the planet at $0.02''$ spaxel⁻¹ (see Fig. 1), where spaxel refers to one OSIRIS spatial resolution element. OSIRIS is an integral field spectrograph that uses a grid of lenslets in the focal plane to dissect the field of view (FOV). The light from each lenslet is dispersed by a grating, producing an array of spectra that are reassembled in the data reduction pipeline (DRP) to a $[x, y, \lambda]$ data cube. A series of 21 *H*-band and 18 *K*-band 900 second exposures were obtained. Appropriate dark, sky, and A0 telluric standard star observations were also obtained. See Table 1 for a summary of these observations.

The OSIRIS DRP was used to produce basic calibrated data (BCD), and includes spatial rectification of the raw data, wavelength and dispersion solutions, sky subtraction, cosmic ray rejection, and so forth (Krabbe et al. 2004). On all three nights in 2009, OSIRIS was operating above its normal detector temperature ($\sim 68\text{K}$). On July 22, the temperature was $\sim 79\text{K}$, but holding steady. On July 23, the temperature was $\sim 80\text{K}$ and also stable throughout the night. However, on July 30, the temperature was not stable and increased from 83.56K at the beginning of the observations to 84.54K at the end. During this period of unstable temperatures, the detector noise in the dark frames increased exponentially. To avoid taking 900 sec sky and dark frames repeatedly throughout the night, “scaled darks” were generated for each 900 sec exposure on the science target by scaling actual darks taken at the beginning and end of the half-night. An exponential function was fit to the total counts in each actual dark from all three nights and, using this function, scaled darks were generated for the science-target cubes on July 30. In 2010, OSIRIS was functioning perfectly, and the observing conditions were excellent.

The final BCD data cubes were, at every spatial position, divided by the spectrum of an A0 standard star and multiplied by a black body ($T = 9600\text{K}$). The spectrum of the A0 star was extracted from its data cube by fitting a 2D-Gaussian at every monochromatic image-slice, rather than using the fixed-aperture extraction routine

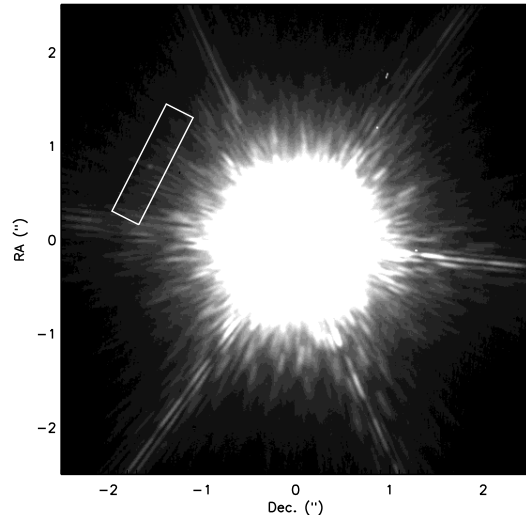


FIG. 1.— An unprocessed NIRC2 image (20 second exposure) of HR8799. The rectangle shows the orientation and size of the OSIRIS spectrograph FOV ($0.02''$ scale). HR8799b is barely visible in the center of this rectangle and comparable in brightness to the speckle contamination. Dithering was done along the long-axis of the FOV.

in the OSIRIS DRP. BD+14 4774 was discovered to be a binary ($0.07''$ separation) with a likely mid to late-type companion; for this star a two-component Gaussian PSF was used to extract the A0 fluxes. The final BCD are cubes with wavelength and two spatial dimensions. At both *H* and *K* bands, the planet was clearly visible in all median-collapsed cubes (median along wavelength). The nominal resolving power of OSIRIS is $R \sim 4000$ with 1600 wavelength channels. However, to improve the signal-to-noise ratio, the BCD cubes were binned to 25 wavelength channels, down to $R \sim 60$. The wavelength positions of OH sky-lines and telluric star features were measured and no artificial wavelength shifts were discovered; a potential concern given the temperature variations encountered during the observations ¹.

While the planet is easily detected in all of the BCD cubes, contamination by scattered star light remains a concern. Figure 1 shows the FOV and orientation for the OSIRIS observations and the extent of speckle contamination in the observed region. Since the spatial scaling of the speckles, radially from the star, is proportional to λ , speckles can intersect the spatial location of the planet in a wavelength-dependent manner. To suppress the speckle pattern, each BCD cube was processed with custom IDL routines that first subtracts a (spatially) low-pass filtered version of the image slice in each wavelength channel and rebins the data cube (by taking the median in the λ dimension) to 25 wavelength channels ($R \sim 60$). Each monochromatic image-slice of this rebinned cube is magnified about the stars position by λ_m/λ , where λ_m is the median wavelength in either *H* or *K* band. In these shifted data cubes, individual speckles align and are fit with simple polynomial functions of λ . Prior to this step,

¹ Several updates of the OSIRIS DRP became available during the course of this work; one of these was directly related to preventing unwanted wavelength shifts (<http://irlab.astro.ucla.edu/osiris/>).

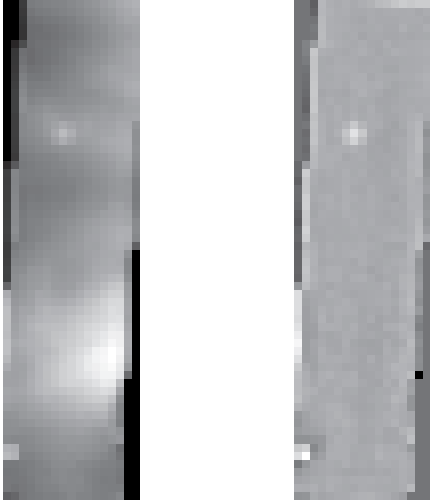


FIG. 2.— *Left*: A single H -band basic calibrated data cube (900s exposure at one dither position), median combined along the wavelength dimension. The planet is visible in the upper left quadrant. Bright speckles are visible across most of the image. The image is oriented such that the star is to the right. *Right*: Same data as in the left panel, but after speckle-suppression.

the planet is masked to avoid biasing the polynomial fit. The final polynomial fits to the speckle fluxes are subtracted from the shifted cube before finally reversing the magnification of the cube, placing the planet back in its original position. Collapsed H -band data cubes, before and after speckle removal, are shown in Fig. 2 (a similar improvement is seen in the before and after K -band data cubes). The speckle suppression scheme described here is similar to that used for the low-mass companion GQ Lupi b (McElwain et al. 2007); however, McElwain et al. did not rescale the cubes for speckle fitting but instead fit the underlying speckle halo in each spectral bin of the data cube since each spatial location is more than critically sampled.

The speckle suppression steps described above contain two important variables: the size of the masked region (centered on the planet) and the order of the polynomial used to fit the speckle fluxes. To determine the best pair of parameters, ten fake planets (similar in brightness and FWHM as the real planet but with constant F_λ) were inserted into the BCD data cubes, evenly spaced but avoiding the real planet location as well as the edges of the FOV. These cubes were processed using the twelve combinations of four mask radius values (from 0.5 to 2 in 0.5 spaxel steps) and three polynomial orders (1, 2 and 3). The parameters resulting in extracted fake planet spectra with the smallest mean deviation from a flat line and smallest $\text{RMS}(\lambda)$ were mask radii equal to 1.5 and 2.0 for H and K bands respectively and a polynomial order equal to 1 for both bands. The mean residuals of all ten fake planet spectra are shown in Fig. 3, straddling zero flux. The $\text{RMS}(\lambda)$ for the fake planet spectra were comparable to, or smaller than, the final uncertainties adopted for the planet spectrum, providing confidence that the errors have not been significantly underestimated. Furthermore, the data collected in 2009 compare very well to those from 2010, indicating that the

thermal instabilities and scaled darks had little impact on the final reduced spectra.

The planet fluxes were obtained from the speckle-suppressed data (SSD) cube by convolving each monochromatic image-slice with a two-dimensional, Gaussian, point-spread-function with $\text{FWHM} = 2.2$ (H -band) and 2.7 (K -band) spaxels. The final spectra were flux calibrated using H -band (Metchev et al. 2009) and a revised K_s magnitudes (discussed below). The final extracted spectra and corresponding error-bars (taken as the RMS of all the extracted spectra in each band-pass) are shown in Fig. 3 and listed in Table 2.

As can be seen from the residuals of the fake planet fluxes (Fig. 3), the noise in the spectra is correlated between different wavelengths. This is a natural consequence of the fact that the noise is primarily from the speckle pattern - the typical speckle has a monochromatic size of λ/D , as does the extraction box for the planetary spectrum. A single speckle's position scales with wavelength proportional to λ . At K band, the planet is located approximately $42 \lambda/D$ from the star. For the speckle to move completely across the extraction box requires a change in wavelength of $(43/42-1) \times 2.1 \mu\text{m} = 0.05 \mu\text{m}$. Hence speckle noise patterns will be correlated across the spectrum over a range of $0.05 \mu\text{m}$ (Sparks & Ford 2002). In principle this should be formally accounted for in the estimate of χ^2 when fitting models to the data (described below). However, since the spectral features being fit are also of width $\sim 0.05 \mu\text{m}$ or larger, the correlations in the noise have been ignored.

The planet spectra, before and after speckle suppression, are also compared in Figure 3. Near $1.7 \mu\text{m}$, the impact of a bright speckle can be seen as a fairly sharp peak spanning two wavelength channels. Speckle noise and photon noise are roughly equal in these data sets at this binning, so speckle suppression improved the SNR by approximately 50%. Most importantly, the speckle noise that was removed was spectrally correlated across multiple channels and non-Gaussian, e.g. the feature at $1.7 \mu\text{m}$ in Figure 3, and would have a much more significant effect on the final interpretation than the white photon noise.

2.2. Photometry

On August 7 2009 (UT), when OSIRIS was too warm to operate, an angular differential imaging (ADI, Marois et al. 2006) sequence was taken with NIRC2 using four narrow-band filters in the K -band window (see Table ??). These filters were selected to sample, as uniformly as possible, the full K -band region accessible with OSIRIS and thus serve as a consistency check on the shape of the final, fully processed, OSIRIS spectrum. These narrow-band data are compared in Figure 3 to equivalent flux points obtained from the OSIRIS data convolved with the filter response profiles. The NIRC2 narrow-band colors are consistent with the OSIRIS spectral shape on either side of the peak flux; however, HeIB ($2.06 \mu\text{m}$) photometry is only consistent at $\sim 2\text{-}\sigma$. The overall agreement, between these two non-contemporaneous data sets, processed with different reduction software, provides some confidence that the planet's spectrum was faithfully extracted from the speckle-contaminated data.

Also in 2009, new CH_4 (4% S/L) photometry was

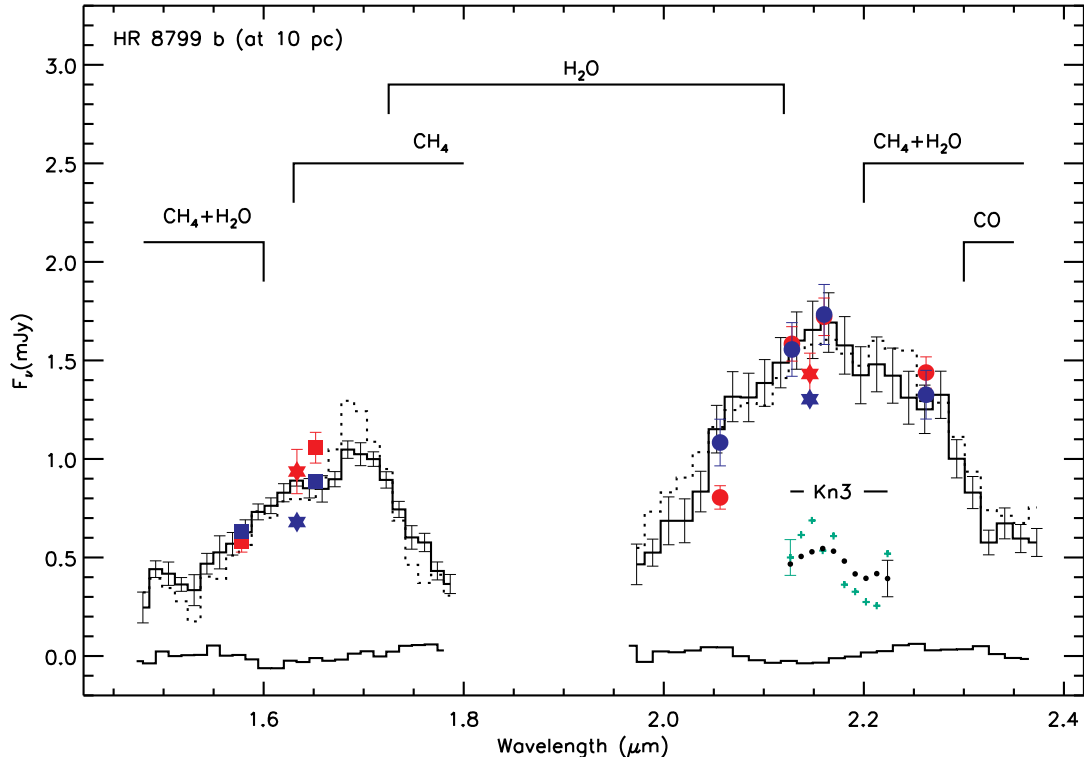


FIG. 3.— OSIRIS H and K -band fluxes of HR8799b (scaled to 10 parsecs) plotted with $1\text{-}\sigma$ uncertainties. The location of prominent water, CH_4 , and CO absorption bands are indicated. The fluxes extracted without the speckle suppression algorithm are shown as dotted lines. The bottom two curves are the mean residuals of fake planets with flat spectra extracted from the same data cubes (see text for details). The Kn3 spectrum of Bowler et al. (2010) is shown as green pluses (scaled arbitrarily down) over plotted with the broad-band spectrum (black points) interpolated onto the Bowler et al. Kn3 wavelength points. The mean $1\text{-}\sigma$ uncertainties across the Kn3 range are shown at either end for each data set. The larger red filled symbols are the NICI CH_4 short/long (boxes), NIRC2 narrow (circles), and NIRC2 broad-band (stars) photometry taken from Table ???. Blue symbols are the corresponding photometry derived from the OSIRIS spectra.

TABLE 2. OSIRIS H AND K SPECTRA (SCALED TO 10 PARSECS)

λ	F_ν (mJy)	error ($1\text{-}\sigma$)	λ	F_ν (mJy)	error ($1\text{-}\sigma$)
1.48	0.25	0.08	1.97	0.47	0.10
1.49	0.44	0.04	1.99	0.52	0.07
1.50	0.42	0.06	2.00	0.69	0.12
1.52	0.36	0.03	2.02	0.69	0.11
1.53	0.33	0.08	2.04	0.83	0.10
1.54	0.47	0.05	2.05	1.15	0.12
1.56	0.53	0.08	2.07	1.32	0.13
1.57	0.57	0.06	2.08	1.31	0.12
1.58	0.63	0.06	2.10	1.39	0.12
1.59	0.73	0.04	2.12	1.49	0.13
1.61	0.76	0.04	2.13	1.60	0.15
1.62	0.83	0.05	2.15	1.66	0.15
1.63	0.89	0.03	2.16	1.69	0.15
1.65	0.85	0.05	2.18	1.58	0.15
1.66	0.85	0.07	2.20	1.42	0.14
1.67	0.90	0.04	2.21	1.48	0.14
1.68	1.05	0.04	2.23	1.42	0.14
1.70	1.02	0.06	2.24	1.31	0.13
1.71	1.00	0.04	2.26	1.25	0.12
1.72	0.89	0.04	2.28	1.33	0.12
1.74	0.74	0.04	2.29	1.00	0.10
1.75	0.60	0.06	2.31	0.83	0.08
1.76	0.58	0.05	2.32	0.58	0.06
1.77	0.43	0.05	2.34	0.67	0.08
1.79	0.37	0.05	2.36	0.60	0.07

obtained with the Near Infrared Coronagraphic Imager (NICI; Toomey et al. 2003) on Gemini South. The NICI CH_4 short/long filters more optimally probe the strength of CH_4 absorption than the NIRC2 CH_4 short/long filters. The former are narrower, have less overlap, and have central wavelengths that correspond well to the min and max fluxes seen in H -band spectra of mid to late T dwarfs. A comparison between these new photometric data and equivalent band-integrated flux points from the OSIRIS spectrum is shown in Fig. 3. Here again the CH_4 short/long slope is in excellent agreement with the OSIRIS spectrum.

Since the discovery of the HR8799 planetary system more broad-band observations have been published and improvements have been made in the LOCI (Lafrenière et al. 2007) and ADI algorithms (at least those used by this group). For the analysis presented here, the H -band photometry of Metchev et al. (2009) has been adopted. Also, K_s data taken in 2010 have been analyzed and a new K_s magnitude ($M_{K_s} = 14.15 \pm 0.1$) has been obtained. See Table ?? for a full list of the NIRC2 and NICI photometry used in this study.

2.3. Comparison to Kn3 spectrum

On June 21st (UT) 2009, Bowler et al. (2010) observed HR8799b using the OSIRIS Kn3 narrow-band filter. A

TABLE 3. NIRC2 AND NICI PHOTOMETRY

Filter	λ_c	Mag	F_{10pc} (mJy)	ZP(Jy)	Ref
NIRC2 broad-band					
J	1.25	16.30	0.46 ± 0.07	1521.1	Mar08
H	1.63	15.08	0.94 ± 0.11	1010.0	Met09
K_s	2.15	14.15	1.43 ± 0.11	654.2	updated
L'	3.78	12.66	2.06 ± 0.21	238.5	Mar08
NICI narrow-band					
CH_{4short}	1.59	15.18	0.88 ± 0.14	1035.7	new
CH_{4long}	1.68	14.89	1.06 ± 0.18	959.7	new
NIRC2 narrow-band					
He I B	2.06	14.73	0.85 ± 0.07	665.9	new
$H_2(v=1-0)$	2.13	14.16	1.52 ± 0.11	703.4	new
$Br_{\gamma 2}$	2.16	13.93	1.66 ± 0.12	618.9	new
$H_2(v=2-1)$	2.26	14.09	1.37 ± 0.11	593.5	new

Mar08 = Marois et al. (2008); Met09 = Metchev et al (2009)

comparison between the narrow and broad-band spectra is shown in Fig. 3, and both spectra agree within the $1-\sigma$ error-bars. The Bolwer et al. spectrum decreases in flux more noticeably than the broad-band spectrum; Bolwer et al. attribute this decrease in flux to possible weak CH_4 absorption. The broad-band spectrum, which encompasses much more of the CH_4 absorption band, indicates an even weaker CH_4 signature than indicated by the Kn3 spectrum.

3. EMPIRICAL COMPARISONS

The H and K -band spectra of HR8799b show several interesting features. In the H band, a pronounced triangular shape indicative of weak collision induced absorption (CIA) and low surface gravity is seen. The spectrum also shows no evidence of strong methane absorption (consistent with CH_4 on/off photometry) as would otherwise be expected in cold T-type brown dwarfs. At K band, the spectrum shows very deep water absorption bands. As in the H band, there is no evidence of strong methane absorption or very strong CO absorption.

HR8799b occupies sparsely populated regions of near-IR color-magnitude diagrams. Despite this fact, it is still useful to compare the observed spectra of HR8799b to those of known brown dwarfs. Figure 4 compares the H and K -band spectra to a sequence of L and T dwarf spectra from type T6 to L1. The near-IR spectrum HR8799b is fairly distinct from these typical field brown dwarfs, which generally have weaker water absorption and, for the T dwarfs, have deeper CH_4 absorption than seen in HR8799b. The fact that none of the hotter, L-type, brown dwarfs provide a good match to HR8799b is consistent with the low effective temperature deduced from cooling track models (Marois et al. 2008).

Brown dwarf near-IR colors exhibit considerable spread within a given spectral type and a number of peculiar (anomalously red or blue) L and T dwarfs are turning up (Kirkpatrick et al. 2008; Burningham et al. 2010). Consequently, while standard BDs do not match HR8799b very well, perhaps some of the more peculiar BDs might. The SpeX Prism spectral library² provides

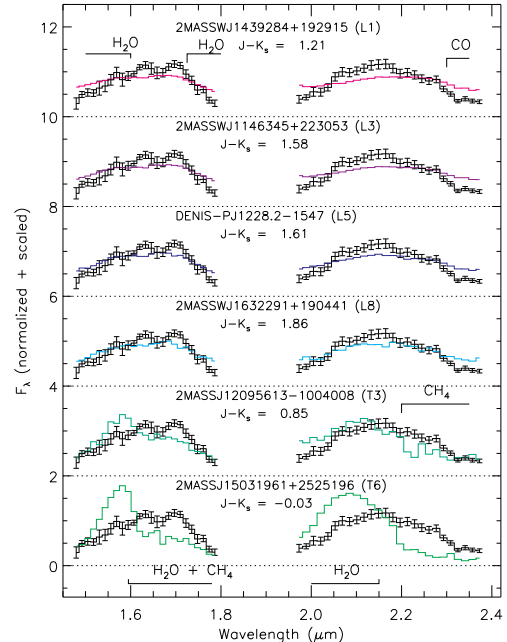


FIG. 4.— OSIRIS H and K -band spectra of HR8799b (plotted as F_λ) compared to field brown dwarf spectra (taken from the SpeX spectral library). Each band was normalized individually; the actual $J-K_s$ color is given below each object name. All of these field objects are bluer than HR8799b.

over 300 low-resolution L and T dwarf spectra from ~ 0.65 to $2.55 \mu m$ and includes a number of very red T dwarfs. These spectra were rebinned to match the resolution and sampling of the HR8799b OSIRIS spectra and used to find the best match to the H and K band spectra separately by minimizing χ^2 . All L and T dwarfs available in the SpeX library were used, except known binaries.

Figure 5 shows the results of fitting the SpeX observations to HR8799b. There is a clear χ^2 minima between T0 and T2, with the best fitting objects having spectral types T1.5 and T0.5 for the H and K bands, respectively (within the range found by Bowler et al., who fit their Kn3 spectrum to the same SpeX library). An empirical fit to the broad-band photometry was also performed by Bowler et al.; their best overall match (a peculiar L6 2MASS 2148+4003) is compared to the H and K -band spectra in Fig. 5. While this L6 is a good match to the broad band photometry, it is not a good match to the broad-band near-IR spectral data.

It is interesting to note that, while fitting brown dwarf spectra is completely independent of how well the broad-band colors agree (each band was normalized individually for the χ^2 calculation), there is a clear correlation between $J-K_s$ color and χ^2 . At first glance, this is simply restating that the best fits are found among the late L and early T dwarfs, which have the reddest $J-K_s$ colors. However, in this case, the best fitting objects are noticeably redder than the mean $J-K_s$ color for their spectral type. The lower panel of Fig. 5 shows χ^2 versus $J-K_s$ color for all T dwarfs. For both bands, the best fitting objects (a T0.5 and a T1) are redder than the mean $J-K_s$ for T0 to T2 (vertical dotted lines, values taken from

² <http://web.mit.edu/ajb/www/browndwarfs/spexprism>

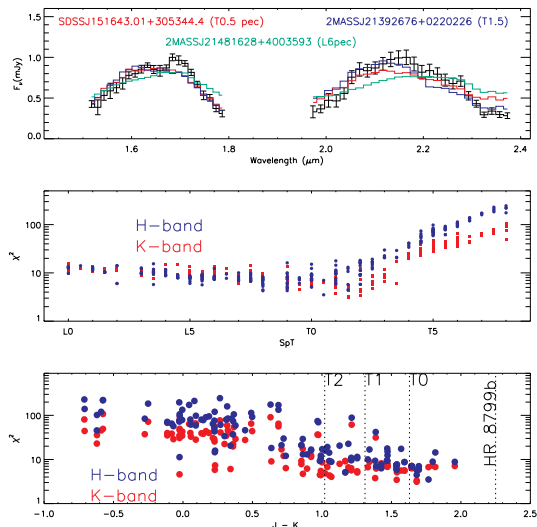


FIG. 5.— *top panel*: real brown dwarf spectra that best fit the H and K bands of HR8799b separately (red: best fit to H band, blue: best fit to K band). Each spectrum is scaled arbitrarily to have the same total normalized flux. Plotted in green is the spectrum of 2MASS J2148+4003, the object found by Bowler et al. (2010) to be the best overall match to HR8799b. *middle panel*: χ^2 values versus spectral type for real brown dwarfs compared to H (blue) and K (red) bands. *bottom panel*: χ^2 values versus $J - K_s$ color for real T-type brown dwarfs compared to the H (blue) and K (red) bands. Vertical dotted lines indicate the $J - K_s$ color for HR8799b as well as typical colors for field T0, T1, and T2 dwarfs.

Faherty et al. 2009). While none of the objects available in the SpeX library are as red as HR8799b, there is a clear indication that early T dwarfs, with anomalously red near-IR colors, are the best match. This trend was also independently noted by Bowler et al.

The best fit for H band, SDSS J151643.01+305344.4, (here after SDSS 1516+30), has $J - K_s = 1.77$ and has been classified as $T0.5 \pm 1$ (Chiu et al. 2006; Burgasser et al. 2006) and $T1.5 \pm 2$ (Burgasser et al. 2010). While SDSS 1516+30 matches HR8799b in H band very well, the comparison is poor at K band. Stephens et al. (2009), fitting their model atmospheres to available near-IR and mid-IR spectra of SDSS 1516+30, found $T_{\text{eff}} = 1000$ to 1100 K, $\log(g) = 4.5$ and a fairly cloudy atmosphere for such a low T_{eff} ($f_{\text{sed}} = 1$ to 2, in the Ackerman & Marley (2001) parlance). This T_{eff} range is lower than typical for a T0.5, by 200 to 300K (Stephens et al. 2009; Golimowski et al. 2004). Burgasser et al. (2010) identify SDSS 1516+30 as a weak, if not unlikely, binary candidate; however, binarity has yet to be tested with high resolution imaging. Leggett et al. (2007) have also noted this object’s mid-IR colors are best reproduced by models with thick clouds and stronger CO absorption than predicted by pure chemical equilibrium, consistent with the high eddy diffusion coefficient used by Stephens et al. in their model comparison.

The best fit for K band is 2MASS J21392676+0220226 (here after 2M2139). The brown dwarf has $J - K_s = 1.68$ and has been classified as T0 (Reid et al. 2008), T1.5 (Burgasser et al. 2006), and recently as $T2.5 \pm 1$ (Burgasser et al. 2010). Not only does 2M2139 match HR8799b reasonably well in the K band, the comparison is also about as good as SDSS 1516+30 in the H band.

Burgasser et al. (2010) suggest that this object is a strong binary candidate, though no high-resolution imaging has been reported. It is quite possible that the object is single and simply non-standard with atmospheric properties that are a mix of those found in the cloudy and cloud-free brown dwarf photospheres. The K -band spectrum of 2M2139 is similar to that of SDSS J0758+42 (a T2), the brown dwarf found by Bowler et al. that best matched their Kn3 spectrum. The H -band spectrum of SDSS J0758+42, however, is noticeably bluer than the HR8799b OSIRIS H -band spectrum.

In summary, the empirical comparisons suggest a spectral type of $T1 \pm 1$, consistent with the T2 match that Bowler et al. (2010) found when comparing their Kn3 spectrum to the SpeX library. However, it appears as though only the reddest T dwarfs in this spectral type range provide reasonable matches to the HR8799b spectra. While a T1 is a close match, the near-IR colors of HR8799b are still well out of the normal range for this spectral type (being more consistent with the mid L dwarfs; consequently, there are probably significant limitations to what any near-IR spectral type can tell us about the basic properties of HR8799b.

4. MODEL ATMOSPHERES

Recognizing that HR8799b falls outside of the color-magnitude range of most known substellar objects, comparing the observed data to synthetic spectra from model atmospheres is the next logical step. The PHOENIX model atmosphere code (Hauschildt et al. 1997) has been used to explore a variety of physical mechanisms that might explain the unusually red near-IR colors, low luminosity, and lack of strong methane bands. The version of PHOENIX (v16) used here has been substantially updated since the introduction of the PHOENIX “cond” and “dusty” brown dwarf atmosphere models (Allard et al. 2001). Some, but not all, of the updates include the replacement of the original Allard chemical equilibrium solver with a new, more robust and chemically complete, equation of state³, a revised treatment of pure dust grains, improved alkali line profiles (Allard et al. 2007), and new molecular line lists, most notably for methane (Warmbier et al. 2009; Hauschildt et al. 2009) and water (Barber et al. 2006). Updates to the cloud modeling and the addition of mixing-induced disequilibrium chemistry are the most relevant here and are described in the following sections.

4.1. A Simple Cloud Model

Atmosphere models born from the study of brown dwarfs are commonly used to estimate the properties of giant planets and to estimate detection yields for direct imaging surveys, so it is natural to use such models as starting points for an analysis of HR8799b. Arguably the most complex physical process to include in substellar atmosphere models is the presence of clouds. The term cloud is used here to refer to solid or liquid particles suspended in the atmosphere and, depending on the temperatures and pressures, can include a complex mixture of species ranging from iron particles to ices. The majority of substellar atmosphere models are one-dimensional,

³ The new equation of state routine is known as the Astrophysical Chemical Equilibrium Solver, or ACES (Barman & Hauschildt, in prep).

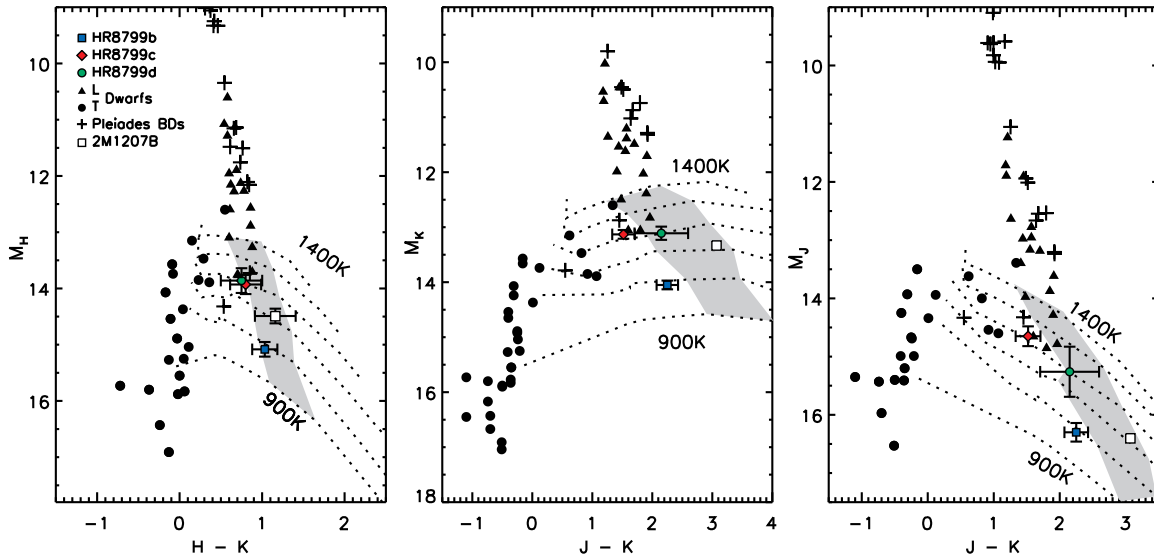


FIG. 6.— Near-IR color-magnitude diagrams for brown dwarfs (Leggett et al. 2002; Knapp et al. 2004; Casewell et al. 2007) and the planets 2M1207b and HR8799bcd. Dotted lines show color-magnitude tracks for chemical equilibrium models of constant T_{eff} (900K to 1400K in steps of 100k, from top to bottom), $\log(g) = 4.0$, and particle size ($10 \mu\text{m}$), but varying cloud thickness increasing from left (no clouds) to right. The shaded region indicates a zone of similar cloud properties; namely where the exponential cloud weighting function begins at similar heights (between $P_{\text{min}} = 1$ and 3 bar). In terms of cloud properties, the young planet-mass objects appear to be an extension of the L-dwarf sequence (see text for more details).

assuming either plane-parallel or spherical geometry, and consequently when clouds are included their spatial properties can only be modeled radially. Nevertheless, the “patchiness” of clouds can be explored in an ad hoc fashion via a combination of cloudy and cloud-free models (Burgasser et al. 2002) or, more recently and self-consistently, within a single one-dimensional model (Marley et al. 2010). For an extensive review and comparison of theoretical cloud modeling in substellar atmospheric conditions, see Helling et al. (2008a).

The observed luminosity and colors of HR8799b have already been shown by Marois et al. (2008) to be inconsistent with those of field brown dwarfs. Therefore, by extension, these data are inconsistent with the predictions of most published substellar atmosphere models, as they are often tuned to match existing observations. A large number of early brown dwarf models reproduced the basic trends of L and T dwarfs by approximating the cloudy and cloud-free conditions in a very simple manner; by simply turning on (cloudy) or off (cloud-free) the opacity of dust in the atmosphere at its chemical equilibrium temperature-pressure location (Allard et al. 2001). This approach, taken to be the extreme limits of cloud influence, is not expected to reproduce every individual object well, especially those in the transition region from spectral types L to T. In fact, most objects should fall between these two limiting cases. In order to match the photometric and spectroscopic observations of HR8799b a different approach is required – a cloud model that is intermediate to these two limits is needed.

Recent improvements in the atmospheric modeling of transition brown dwarfs have been made, with most efforts attacking the cloud problem by adding one or more new parameters that regulate the cloud thickness, particle density, grain size distribution and so forth (Ackerman & Marley 2001; Marley et al. 2002; Tsuji 2005;

Cooper et al. 2003; Burrows et al. 2006). However, see Helling et al. (2008b) for a completely different approach. The purpose of this paper is not to develop a new complex cloud model, but rather to identify the major physical processes that shape the spectral properties of HR8799b. To that end, a simple parameterized cloud model is adopted for the analysis presented here. The lower boundary (cloud base) is established by the intersection of the temperature-pressure (T-P) profile and the relevant chemical equilibrium condensation curve (P_c , using pressure as a proxy for height). The behavior of the cloud above P_c is determined by a single free parameter (P_{min}). The equilibrium dust concentration is multiplied by a function that is 1 for $P_{\text{gas}} \geq P_{\text{min}}$ and decays exponentially for $P_{\text{gas}} < P_{\text{min}}$. If $P_{\text{min}} > P_c$, then the maximum dusty-to-gas ratio is also lowered relative to an equilibrium cloud. Examples of vertical cloud properties are discussed below in more detail. The particle sizes follow a log-normal distribution with a prescribed modal size (a_0) from 1 to $100 \mu\text{m}$ that is independent of height. This cloud model shares some similarities with other parameterized cloud models (Tsuji 2005; Burrows et al. 2006); however, rather than accounting for a small representative set of grains, all thermodynamically allowed grains with opacities in the PHOENIX databases are included in the total cloud opacity; see Ferguson et al. (2005) for a list of grains included in the model.

Figure 6 shows the location of HR8799b relative to L and T brown dwarfs in three near-IR color-magnitude diagrams. Synthetic color-magnitude sequences are also shown for chemical equilibrium models ($K_{zz} = 0$) with radius set to that of Jupiter. Each sequence corresponds to a different T_{eff} (with $\log(g) = 4.0$) and different cloud thickness varying from no clouds (at the blue end) to maximum cloud thickness (at the red end). These sequences of models are not associated with any evolution-

ary cooling tracks since the radius has been arbitrarily set to that of Jupiter. Such sequences illustrate the color trends produced by changing vertical cloud thickness (note this is different from the uniform sinking of clouds). Figure 6 shows that the slope in a CMD across the L-to-T transition region, including the J -band brightening, is reproduced very well by atmospheres that have clouds smoothly decreasing in vertical thickness. However, as pointed out by Burrows et al. (2006), reproducing color-trends does not guarantee good reproduction of near-IR spectra; the models shown in Fig. 6 have not been compared to spectra of field brown dwarfs (an exercise left to another paper).

Figure 6 also shows that very red objects with relatively low luminosities, like HR8799b, can be reproduced by allowing low T_{eff} models (typically assumed to be in the regime of cloud-free photospheres) to have clouds extending across their photosphere. The location of HR8799b, in all three CMDs is intersected by a model with $T_{\text{eff}} = 1000\text{K}$, $\log(g) = 4.0$, and a cloud that starts to fall off near 1 bar of pressure (though the precise P_{min} matching the position of HR8799b is slightly different in each CMD). Figure 6 also suggests that the cloud properties of the HR8799 planets and 2m1207b are similar to the those of late-type L dwarfs. The comparison in Fig. 6 does not directly identify a best fit to the ensemble of data, but simply illustrates the impact that cloud thickness has on the near-IR colors of an object with typical substellar temperatures and gravities and points to a reasonable place to start looking for a good match to HR8799b, namely $T_{\text{eff}} \sim 1000\text{K}$ and $\log(g) \sim 4.0$.

4.2. Disequilibrium Chemistry and Vertical Mixing

The majority of atmosphere models for brown dwarfs and exoplanets assume local chemical equilibrium; in other words, the mole fractions for each chemical compound is determined by the local temperature and pressure, and overall element abundances. For most atmospheric compounds, this is an excellent approximation as the chemical reactions that establish the equilibrium mole fractions are rapid compared to the mixing time scales (even in the convection zone). However, this is not always the case and it has been shown that, for example, the reactions that ultimately replace CO with CH₄ can be very slow in Jovian and brown dwarf photospheres. The same can be true for N₂ and NH₃. Prinn & Barshay (1977) showed that vertical mixing of CO can be important in Jupiter and, later, Fegley & Lodders (1996) predicted that this would also be the case for brown dwarfs. The spectroscopic detections of CO in several cool T-type brown dwarfs (Noll et al. 1997; Saumon et al. 2000, 2006; Geballe et al. 2009) along with weaker than predicted fluxes from $\sim 4.5 \mu\text{m}$ ground and space-based photometry (Patten et al. 2006; Leggett et al. 2007) have established disequilibrium CO mole fractions as a common occurrence in brown dwarfs. Non-equilibrium chemistry is, therefore, a plausible mechanism for the apparently weak CH₄ absorption in HR8799b.

Disequilibrium CO/CH₄ and N₂/NH₃ chemistry has been added to PHOENIX following Smith (1998). The reaction time scales (in seconds) for $N_2 \rightarrow NH_3$ and $CO \rightarrow CH_4$ are from Lodders & Fegley (2002) and Yung et al. (1988), respectively:

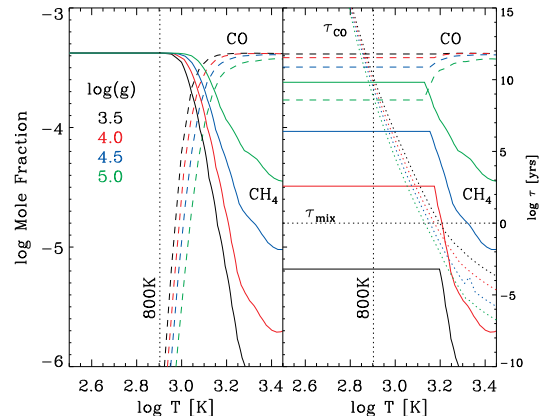


FIG. 7.— CO (dashed lines) and CH₄ (dotted lines) mole fractions for a cloudy, solar metallicity, model atmospheres with $T_{\text{eff}} = 800\text{K}$ and four different surface gravities (corresponding colors indicated in the figure legend). Chemical equilibrium mole fractions are plotted in the left panel. Non-equilibrium mole fractions are plotted in the right panel, where the mole fractions are quenched at different depths determined by the intersection of the CO chemical reaction and mixing time scales (τ_{CO} and τ_{mix} , dotted lines). The latter time scale was arbitrarily set to 1 yr. In both panels, the vertical dotted line marks the approximate location of the photosphere (taken here to be where the local temperature equals the effective temperature).

$$\tau_{N_2} = \frac{1}{\kappa_{N_2} N(H_2)} \quad (1)$$

$$\kappa_{N_2} = 8.45 \times 10^{-8} \exp\left(\frac{-81515}{T}\right) \quad (2)$$

$$\tau_{CO} = \frac{N(CO)}{\kappa_7 N(H) N(H_2CO)} \quad (3)$$

where T is the gas temperature in Kelvin, κ are the rate coefficients in cm^3/sec (with κ_7 interpolated from tabulated values in Yung et al. 1988) and $N(\text{species})$ is the number density of the specified species in cm^{-3} .

The mixing time scale (τ_{mix}) is computed using mixing length theory in the convection zone, and set equal to L_{eff}^2/K_{zz} in the radiative zone, where the effective length scale (L_{eff}) is determined following the recipe in Smith (1998). For the range of models explored here, L_{eff} was found to be ~ 0.1 to $0.2H_P$, with H_P equal to the pressure scale height. This range of L_{eff} is comparable to that found for Jupiter (Smith 1998; Visscher et al. 2010). The major unknown when modeling vertical mixing is the eddy diffusion coefficient (K_{zz}) which, as is frequently done, is assumed here to be an adjustable parameter typically ranging from 100 to $10^8 \text{cm}^2 \text{sec}^{-1}$. With these chemical and mixing time scales, the mole fractions of CO/CH₄ and N₂/NH₃ are “quenched” at a specific depth in the atmosphere where $\tau_{\text{mix}} = \tau_{\text{chem}}$. Below this point in the atmosphere, where $\tau_{\text{mix}} > \tau_{\text{chem}}$, chemical equilibrium prevails. This simple quenched model has been used in several recent studies of brown dwarfs and giant planets (Hubeny & Burrows 2007; Fortney et al. 2008).

The mixing and chemical time scales alone do not determine the final quenched mole fractions, the atmosphere temperatures and pressures still establish these

values at the quenching depth. Consequently, effective temperature, surface gravity, and metallicity play an important role. Of particular importance is the relative location in the atmosphere of equal CO/CH₄ equilibrium mole fractions ($P_{CO=CH_4}$) and where $\tau_{mix} = \tau_{chem}(P_q)$. If $P_q > P_{CO=CH_4}$, the CO/CH₄ ratio can be greater than 1 in cool substellar atmospheres where CO would otherwise be predicted to be orders of magnitude less than CH₄.

As shown in Figure 7, the magnitude of the disequilibrium effect is sensitive to surface gravity, as this quantity acts to shift the locations of P_q and $P_{CO=CH_4}$. As gravity decreases, the crossing point of the radiative and mixing time scales moves to deeper layers (higher T), while the crossing of the equilibrium mole fractions of CO and CH₄ moves outward. For K_{zz} values typically used in brown dwarf models and at low surface gravities expected for young exoplanets, the CO/CH₄ ratio can become significantly greater than 1 – indicating a role-reversal in the dominant carbon-bearing species at photospheric depths. Such a role reversal has not been explored thoroughly in brown dwarfs as their surface gravities and effective temperatures almost always place the time scale crossing point at a pressure lower than that of the equilibrium CO/CH₄ crossing point, resulting in a CO/CH₄ ratio always less than 1 (though still greater than equilibrium chemistry predictions). Hubeny & Burrows (2007) also noted a gravity dependence for non-equilibrium chemistry, but did not explore gravities below $\log(g) = 4.5$ nor encountered a CO/CH₄ reversal. Since a low surface gravity and effective temperature are possible outcomes for HR8799b, a lack of (or very weak) CH₄ could be caused by disequilibrium chemistry.

4.3. Photochemistry

HR8799b is located a mere 68 AU from its host star and receives far too little stellar flux for irradiation to have a significant influence on its atmospheric thermal structure (at near-IR photospheric depths). However, HR8799A is much more luminous ($\sim 5 L_{\odot}$) and hotter ($T_{\text{eff}} = 7500\text{K}$) than the Sun and the UV flux from HR8799A may be sufficient to produce photochemical reactions in the atmosphere of HR8799b and certainly for the inner three planets. Based on a synthetic spectrum from a stellar model atmosphere calculation tailored for HR8799A (also using PHOENIX, with atoms and ions treated in non-local thermodynamic equilibrium), HR8799b is estimated to receive ~ 8 times the flux that Jupiter receives from the Sun for $\lambda < 2000\text{\AA}$, and about 10 times as much flux as Neptune for $\lambda < 3000\text{\AA}$. Given the larger atmospheric temperatures and possibly extreme non-equilibrium CO/CH₄ mole fractions compared to the giant planets in the Solar System, the photochemical reactions in HR8799b will also be quite different from those found in the Solar System. Consequently, photochemistry could impact the model comparisons discussed below. Unfortunately, photochemical reactions are not included in the version of PHOENIX used here. Future observations and modeling will be needed to address this possibility.

5. MODEL COMPARISONS

The complete set of HR8799b broad-band photometry covers a broader wavelength range than the OSIRIS

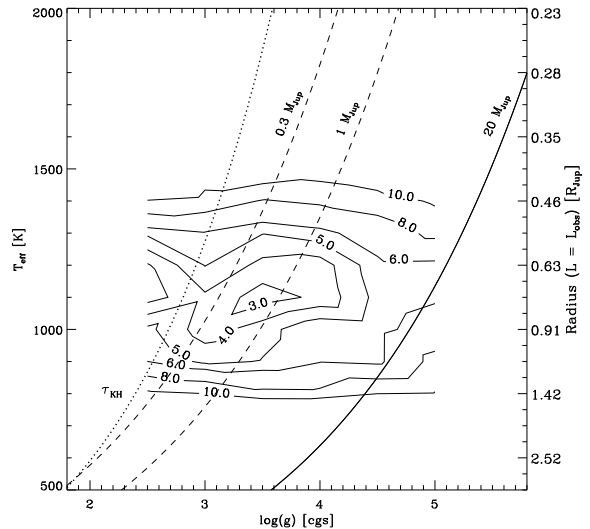


FIG. 8.— Mean χ^2 contours obtained by comparing model spectra to the broad-band photometry (Table 2) and OSIRIS *H* and *K* spectra (Table 3). The best fitting model has $T_{\text{eff}} = 1100\text{K}$ and $\log(g) = 3.5$. The right ordinate indicates the radii required to match the observed luminosity of HR8799b given the effective temperatures on the left ordinate. Using these radii and the surface gravities along the abscissa, lines of constant mass can be plotted (dashed lines for 0.3 and 1 M_{Jup} , solid line for 20 M_{Jup}). These lines of constant mass are *independent* of atmosphere or evolution model predictions. Points along the dotted line are consistent with a Kelvin-Helmholtz cooling time of 1 Myr.

spectroscopic observations and, therefore, are likely to provide the greatest leverage when estimating effective temperature and, potentially when estimating the cloud properties. Marois et al. (2008) did not perform a model fit to the discovery photometry but, rather, focused on the parameters inferred from theoretical cooling tracks and the observed luminosity and age range. With new and improved photometry available, new model fits to these data are now warranted (see Bowler et al. (2010) and Currie et al. (2011) for independent model comparisons to similar photometric data and different model atmospheres). Additionally, the near-IR spectra are likely to contain the greatest information on surface gravity, chemical composition (via broad-band absorption features), and also on the cloud properties. The goal in this section is to identify a single model atmosphere that best fits all three observational data sets and to understand what physical mechanisms play dominant roles in shaping the overall spectral energy distribution.

5.1. Solar Abundance Model Comparison

The cloud and disequilibrium chemistry models described above were incorporated into PHOENIX. A modest grid of synthetic spectra was computed with five key parameters considered: T_{eff} [= 800K – 1500K, 100K increments], $\log(g)$ [= 2.5 – 5.0, in 0.5 increments and CGS units], $K_{zz} = 10^4 \text{ cm}^2 \text{ s}^{-1}$, P_{min} [= 10^5 , 10^6 , 2×10^6 , 4×10^6 , 6×10^6 , 8×10^6 , 1×10^7 dynes cm^{-2}], a_0 [= 1, 5, 10, 100 μm]. Solar abundances were adopted for this grid (Asplund et al. 2005), but the question of non-solar metallicity will be discussed below.

Given the large number of free parameters and the sparse sampling of the model grid, obtaining a traditional

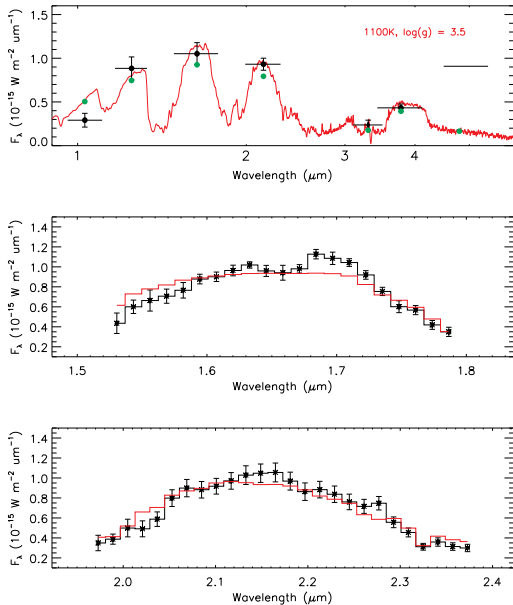


FIG. 9.— Comparison between the best fitting solar-abundance model and the broad-band photometry (top panel) and OSIRIS broad-band H and K spectra (middle and bottom panels). Observations are shown in black with $1\text{-}\sigma$ error bars, the model spectrum in red and model photometry in green. The photometric upper limit from Hinz et al. (2010) is plotted as a horizontal bar.

fit by χ^2 minimization that samples a continuous distribution of parameters is beyond the scope of this paper. Instead, a χ^2 was computed for each model spectrum from the grid compared to each of the three data sets (photometry, H and K -band spectra). When computing a χ^2 for the photometric comparison, each model spectrum was convolved with the appropriate filter response functions to produce synthetic photometry in J , H , K_s , and L' bands along with the filters used by Hinz et al. (2010) and Currie et al. (2011); M_{bar} , z , and a filter centered at $3.3 \mu\text{m}$. When comparing models to the OSIRIS spectra, the synthetic spectra were first smoothed (with a Gaussian kernel) to the native instrumental response for OSIRIS ($R \sim 4000$), then binned down to the same wavelength sampling (and in the same manner) as done for the OSIRIS data cubes. The best fitting model was taken to be the model with smallest mean χ^2 for the three data sets. Figure 8 shows the mean reduced- χ^2 distribution across T_{eff} and $\log(g)$ for the model comparisons to all three sets of data. The best fit is located at $T_{\text{eff}} = 1100\text{K}$ and $\log(g) = 3.5$. Formal error-bars for the fit have not been determined; however, models within the mean $\chi^2 = 4$ contour are all reasonable fits to the data. Therefore, the error on the fit is close to $\pm 100\text{K}$ for effective temperature and ± 0.5 dec for surface gravity, and comparable to most brown dwarf model fit uncertainties found in the literature.

Figure 9 compares the best fit to each of the three data sets. The model spectrum agrees very well with the photometry. The differences seen at J , H , K_s , and L' are within the $1\text{-}\sigma$ error bars. The model only slightly under predicts the flux at $3.3 \mu\text{m}$, compared to the Currie et al. (2011) detection. The flux measurement at $3.3 \mu\text{m}$ excludes a large number of models, especially at high

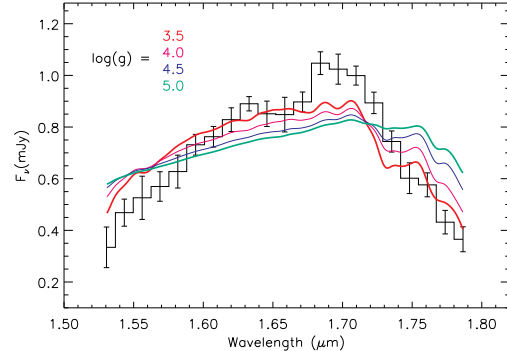


FIG. 10.— Model gravity sequence compared to the OSIRIS H -band spectrum. All model parameters are identical to the best fitting model shown in Fig. 9 except for gravity, which varies from $\log(g) = 3.5$ to 5.0 (cgs units). The triangular shape of the H -band is best explained by low surface gravity.

T_{eff} , and is quite sensitive to the presence or absence of CH_4 . Observations of other systems (e.g., 2M1207b) in this band-pass would be very useful.

At H band, the model spectrum is marginally consistent with the observed spectrum. The slope at the red and blue ends are not as steep as observed and, overall, the model spectrum is too flat. It is possible that the residual flux from the bright speckle feature seen near $\sim 1.7 \mu\text{m}$ (see Fig. 3) remains in the final observed spectrum and is responsible for the larger disagreement seen at this wavelength. As for the red and blue H -band slopes, these wavelength regions have historically been difficult to fit mainly due to missing CH_4 line opacity. Consequently, the level of disagreement at H -band is not too surprising. At K band, the model compares favorably to the observed spectrum. The red and blue slopes are in good agreement as is the location of the peak flux.

When the data sets are compared to the models individually, slightly different results are obtained. The best fitting model to the photometry has $T_{\text{eff}} = 1000\text{K}$ and $\log(g) = 5.0$. H band is best fit by a model with $T_{\text{eff}} = 1200\text{K}$ and $\log(g) = 3.0$ (clearly favoring low gravity); however, this model has colors that are too blue when compared to observed photometry, especially in the z -band. At K band, the best fit has $T_{\text{eff}} = 1100\text{K}$ and $\log(g) = 3.0$. When the mean χ^2 for H and K is minimized, the best fit is $T_{\text{eff}} = 1200\text{K}$ and $\log(g) = 3.5$. Each of these best fit models has a slightly different cloud thickness, but all have $K_{\text{zz}} = 10^4 \text{ cm}^2 \text{ s}^{-1}$ and $a_0 = 5 \mu\text{m}$.

5.2. Inferred Atmospheric Properties

Despite the imperfect fit to the H -band, there is strong evidence for low surface gravity. In Figure 10 the H -band OSIRIS spectrum is compared to a sequence of model spectra with different gravities but with all other parameters equal to those of the overall best fit shown in Fig. 9. The observed triangular shaped pseudo-continuum is best reproduced by the lowest-gravity model. The shape of the H band is often used as a gravity indicator in L-type brown dwarfs, where low gravity objects have distinct triangular spectra (Lucas et al. 2001; Kirkpatrick et al. 2006) compared to the more rounded spectra of older, higher gravity, field brown dwarfs. This

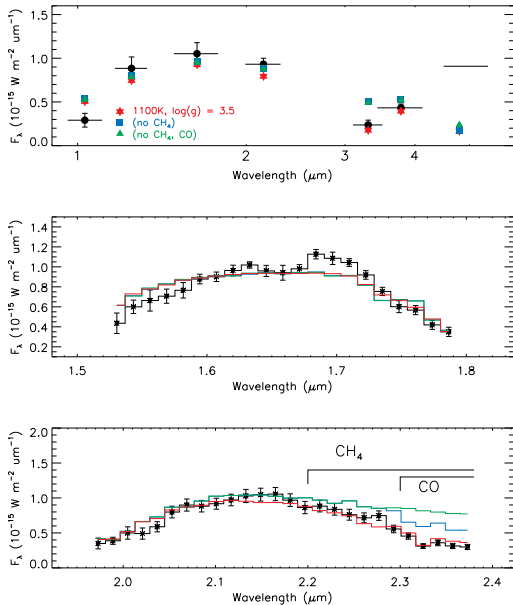


FIG. 11.— Same, best fitting model as shown in Fig. 9 (red), compared to models with the same parameters and temperature-pressure profile, but with CH_4 opacities removed (blue) or both CO and CH_4 opacities removed (green).

gravity-dependence of the H -band is produced by weakening of the continuous opacity produced by collision-induced absorption (CIA) as gravity decreases, relative to the molecular line opacity (most significantly relative to that of H_2O). When CIA is weak, the H -band shape is defined by the natural triangular shape of the H_2O bands on either side of $\sim 1.7\mu\text{m}$. However, when the surface gravity is high, the larger pressures increase the CIA to a point where it can become the dominate opacity source between the two H_2O bands on either side of the peak. The smooth wavelength dependence of CIA rounds the H -band peak (Borysow et al. 1997; Kirkpatrick et al. 2006; Rice et al. 2011). For field brown dwarfs, the effectiveness of H -band as gravity indicator is decreased for field T dwarfs as CH_4 opacity dominates the near-IR and competes with that of H_2O around the H band. However, if CH_4 mole fractions are reduced by vertical mixing and non-equilibrium chemistry at low gravity and low T_{eff} , as is likely the case for HR8799b, then the behavior of the H band with gravity seen in hotter L-dwarfs will persist even down to effective temperatures most often associated with T-dwarfs.

Water is by far the main molecular opacity source shaping the OSIRIS spectra. The combination of high K_{zz} and low $\log(g)$ leads to, in the models used here, a sharp reduction in the CH_4 mixing ratio (e.g. see Fig. 7) with a correspondingly large increase in the CO mixing ratio. Figure 11 compares the best fit model to those with the same parameters and temperature-pressure structure, but with CO or CH_4 opacities removed. Weak CH_4 absorption is evident in the K band, as is a possible contribution from CO; however, the strongest evidence for CH_4 absorption is the Currie et al. (2011) detection (and Hinz et al. (2010) upper limit) at $3.3\mu\text{m}$ where the flux is clearly suppressed by CH_4 . Unfortunately, the Hinz et al. (2010) upper limit near $4.5\mu\text{m}$ is not sensitive enough to

distinguish between the majority of the models explored here and, therefore, does not provide strong constraints on CO.

The best fitting, solar abundance, atmosphere model for HR8799b (shown in Fig. 9) has a cloud base just below $P = 1$ bar with a composition that is typical for brown dwarf models with $T_{\text{eff}} > 1000\text{K}$. Magnesium-silicate (e.g. forsterite) and iron grains are the most abundant, with a mixture of other grains with lower mole fractions. The structure of the cloud has many characteristics in common with brown dwarf cloud predictions, namely an abrupt drop in the gas-to-dust ratio at higher pressures and temperatures, where condensation is no longer thermodynamically favored. This cloud base is determined by the intersection of the T-P profile and the relevant condensation curves (see Fig. 12). At lower temperatures and pressures, the gas-to-dust ratio drops exponentially (by design in this study, see lower panel of Fig. 12) in a similar manner as the smooth decrease in dust predicted by the models of Helling & Woitke and Marley & Ackerman (see Helling et al. (2008a) for a comparison). Location and vertical extent are the most important aspects of the cloud structure for HR8799b preferred by this work. Generally, the cloud base retreats to larger pressures with decreasing T_{eff} and fixed gravity; however, the low gravity of the best fitting HR8799b model counteracts this trend. As gravity decreases the T-P profile shifts to lower pressure, moving the cloud base along with it. At $\log(g) \sim 3.5$, the cloud base sits near the photosphere with vertical extent that is far less than an equilibrium cloud model (see Fig. 12), but sufficient to produce redder colors than cloud-free brown dwarf models with the same T_{eff} and $\log(g)$.

The modal particle size for HR8799b, favored by this work is around 5 to $10\mu\text{m}$. Grains of this size are within the range predicted by the Marley & Ackerman and Helling & Woitke for models with $T_{\text{eff}} \sim 1000\text{K}$. Both groups predict sizes between 1 and $100\mu\text{m}$ at high pressures (> 10 bar) and sizes that decrease below a micron at low pressures (< 1 bar). Burrows et al. (2006) chose $a_0 = 100\mu\text{m}$ (at the high end of most predictions) for their set of reference model atmospheres arguing that, in general, L-type brown dwarfs are best fit when larger grain sizes are assumed but acknowledged that such large grains make fitting the reddest late L dwarfs difficult. As already discussed above, the observed near-IR spectra of the reddest late L and early T dwarfs come closest to matching the H and K -band spectra of HR8799b and, thus, perhaps it should not be surprising that the best model fits are found among those with smaller grains. However, the simulations of Cooper et al. (2003) predict that particle size should actually increase with decreasing gravity. When comparing grain sizes adopted by different models, it is important to remember that grain size alone does not determine the total cloud opacity – composition also plays an important role. In the cloud model used here a mixture of grains are included in the total opacity and such a cloud can be more opaque than a cloud including opacity from only pure silicate grains of the same size.

6. DISCREPANCY BETWEEN ATMOSPHERE AND EVOLUTIONARY MODELS

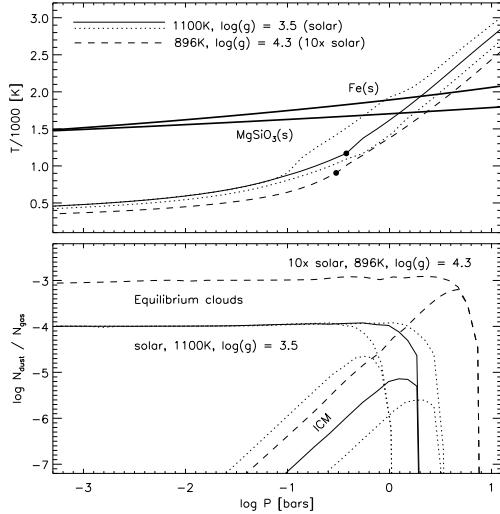


FIG. 12.— *Top* : Temperature versus pressure for the best fitting model identified in Fig. 8 (solid line) and for two models with the same T_{eff} , $\log(g)$ and K_{zz} , but with different cloud model parameters (dotted lines). Also shown (dashed line) is the best fitting metal rich model (Fig. 14). Condensation curves (thick solid lines) for Fe and MgSiO_3 are plotted to indicate the general location of the cloud base, located at the intersection of these curves. Other grains (e.g. Mg_2SiO_4 , Al_2O_3 , Ni, etc.) have condensation curves in same general location. *Bottom* : Dust fraction versus pressure for the same models shown in the top panel (in order from left to right). A constant dust fraction with decreasing pressure is a hallmark of the pure chemical equilibrium cloud (e.g. the ‘DUSTY’ models of Allard et al. 2001). In contrast, the intermediate cloud model (ICM) used here can have lower peak dust fraction than the equilibrium cloud and decays with height (see text for details).

Since the distance to HR8799 has been precisely measured (39.4 ± 1.0 pc, van Leeuwen 2007), the luminosity of HR8799b is known ($\log L_{\text{obs}}/L_{\odot} = -5.1$) and, therefore, radii can be assigned to each T_{eff} value on the left vertical axis of Fig. 8; these radii are given by the right, non-linear, vertical axis. Using these radii and the $\log(g)$ axis values, lines of constant mass can be plotted that are completely independent of interior cooling track models. Dynamical stability arguments suggest that, in order for the three planets to be as massive as indicated by the cooling tracks, they must be in double 2:1 resonances and have masses $\leq 20 M_{\text{Jup}}$ (Fabrycky & Murray-Clay 2010). Using $20M_{\text{Jup}}$ as an upper limit on the mass of HR8799b sets a $T_{\text{eff}}/\log(g)$ boundary in Fig. 8 (right-most solid line). This limit was the motivation for not extending the model grid to $\log(g)$ greater than 5.0. A second boundary, at lower surface gravity, can be set using the Kelvin-Helmholtz time scale (τ_{KH}), which reflects the approximate scaling of detailed planetary cooling curves. Since the planets almost certainly are older than 1 Myr, $\tau_{\text{KH}} = 1$ Myr is a very conservative limit and is indicated by the left-most dotted line in Fig. 8. In other words, planets located to the left of this dotted line could not maintain the observed luminosity of HR8799b for more than 1 Myr (under the usual assumption that the primary energy source is gravitational potential energy). This time scale limit was used to exclude a second minimum at $\log(g) = 2.5$ near $T_{\text{eff}} = 1100$ and 1200K. For $T_{\text{eff}} = 1100\text{K} \pm 100\text{K}$, the radius must be $0.75 R_{\text{Jup}}^{+0.17}_{-0.12}$ to match L_{obs} . Using this radius and the best

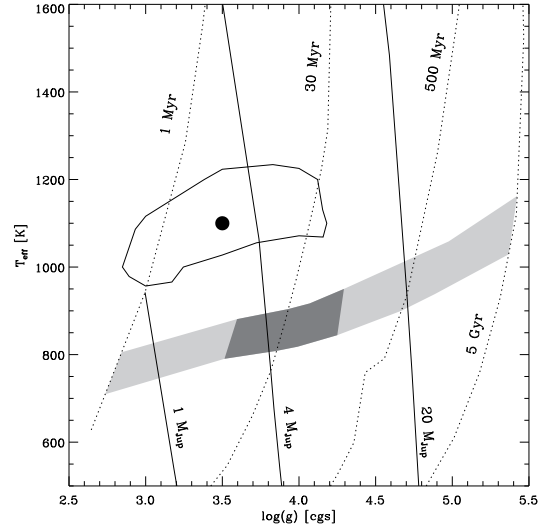


FIG. 13.— Plotted are lines of constant mass (solid) and isochrones (dotted) from Baraffe et al. (2003) cond evolution models. The shaded region covers the range of T_{eff} and $\log(g)$ predicted by these evolution models for an object with the same luminosity as HR8799b (the darker region brackets 10 and 120 Myrs). The best fitting T_{eff} and $\log(g)$, based on fitting solar abundance atmosphere models (see text for details), is indicated by the filled symbol surrounded by the $\chi^2 = 4$ contour from Fig. 8.

fit surface gravity, $\log(g) = 3.5 \pm 0.5$, the corresponding mass is just under 1 Jupiter-mass ($\sim 0.72 M_{\text{Jup}}^{+2.6}_{-0.6}$), a factor of ~ 10 lower than predicted by evolutionary cooling tracks. A radius of $0.75 R_{\text{Jup}}$ is also $\sim 30\%$ smaller than cooling track predictions.

While the implied mass of $\sim 0.7 M_{\text{Jup}}$ is comfortably within the ranged needed for dynamical stability, it is difficult to form objects, either by core-accretion or by gravitational instability, with this mass, radius ($\sim 0.75 R_{\text{Jup}}$), and the planet’s observed luminosity. This combination is inconsistent with our understanding of degenerate or partially-degenerate H+He gaseous bodies with any reasonable heavy-metal composition or of any age (Baraffe et al. 2008). Figure 13 compares the T_{eff} and $\log(g)$ values from the atmosphere model fit to those predicted by evolution models from Baraffe et al. (2003). While the best fit surface gravity is within the expected range, an effective temperature of 1100K is $\sim 300\text{K}$ above the temperatures predicted by all current hot-star cooling tracks, for an age less than 100 Myrs. The high effective temperature would be consistent with evolution predictions if the system was old (> 1 Gyr) and $\log(g)$ was greater than ~ 5 . However, as shown above, such a high surface gravity would be very difficult to reconcile with the H -band spectrum and would have serious dynamical stability implications (Fabrycky & Murray-Clay 2010; Marois et al. 2010; Currie et al. 2011).

Giant planet evolution models are known to become increasingly unreliable at young ages for the simple reason that planet formation is not well understood and, thus, the initial conditions are not known. This fact was highlighted by Baraffe et al. (2002), with a focus on the formation of brown dwarfs and low mass stars from the collapse of molecular clouds (the main realm of applicability for the common cond and dusty cooling tracks).

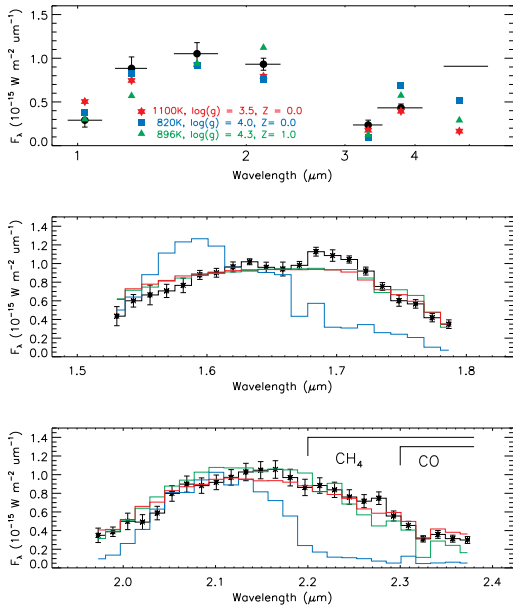


FIG. 14.— Same, best fitting, model as shown in Fig. 9 (red), compared to the best fitting model that has T_{eff} and $\log(g)$ consistent with standard “hot start” evolution models (green). Also plotted are the synthetic spectra and photometry for the chemical equilibrium atmosphere model (blue) from Marois et al. (2008). See text for details.

More recently, Marley et al. (2007) revisited the question of initial conditions by comparing the evolution of planets starting with high T_{eff} and luminosity (“hot start”, as often adopted for brown dwarfs and motivated by the Stahler birth line), to the evolution of planets starting with the colder and less luminous initial conditions (“cold start”) that emerge from core-accretion planet formation models. Marley et al. concluded that young planets that formed by core-accretion are cooler, smaller, and thus fainter than planets formed by single-mode gravitational collapse within a disk or giant molecular cloud. Given that HR8799b is clearly underluminous compared to the hot-start models and overluminous for the cold-start models (Marley et al. 2007; Fortney et al. 2008), it is unlikely that initial conditions alone are responsible for the offset between the atmosphere-inferred properties and the evolution track predictions (a situation similar to that of 2M1207b, as discussed below).

A $\sim 300\text{K}$ offset in effective temperature is similar in magnitude to offsets in effective temperature found for a number of M, L and T-type binary brown dwarfs (Liu et al. 2008, 2010; Konopacky et al. 2010; Dupuy et al. 2010). This suggests that a systematic offset may exist between the atmosphere and interior model predictions. A 10 to 20 % difference in T_{eff} is comparable to the differences between cloudy and cloud-free tracks in the 10 and 100 Myr range and 10 M_{Jup} (Chabrier et al. 2000), so it is still unclear what fraction of such an offset could be resolved by improvements purely in the modeling of the interior or the atmosphere. However, the increasing number of free parameters in substellar atmosphere models is a clear indication that they are even more complex than previously imagined. Thus, the possibility still remains that hidden among the free parameters is an at-

mosphere model with T_{eff} and $\log(g)$ that matches the evolution model predictions.

6.1. Non-solar Abundance Model Comparisons

The need for an intermediate cloud model (constrained vertically), to match the observed broad-band photometry of all three HR8799 planets, was first discussed by Marois et al. (2008). Marois et al. (2008) showed that a synthetic spectrum from a solar abundance model atmosphere with an intermediately thick cloud and $T_{\text{eff}} / \log(g)$ consistent with evolution model predictions (820K / 4.0) matched the available observed photometry at $3\text{-}\sigma$. While only $\text{CH}_{4_{s/l}}$, J , H , K_s , and L' photometry where available in 2008, this earlier (chemical equilibrium) model remains consistent ($\sim 3\text{-}\sigma$) with all of the revised/new broad-band photometry (see Fig. 14). However, the true level of agreement between this model and reality is revealed by the OSIRIS data (Fig. 14) where much weaker CH_4 absorption is observed than predicted by this chemical equilibrium model. This discrepancy highlights the difficulties in obtaining a reliable description of young giant planets from photometry alone, which can hide significant clues about their atmospheric properties.

To explore differences between the atmosphere and evolution derived bulk parameter more closely, a separate grid of atmosphere models was computed, with T_{eff} and $\log(g)$ uniformly sampling the evolution track predictions that are consistent with the observed luminosity of HR8799b (down the center of the grey band in Fig. 13). The clouds and non-equilibrium chemistry were modeled in the same manner as in the solar abundance grid described above, yet only $a_0 = 5$ and $10 \mu\text{m}$ were used. The metallicity, however, was extended beyond solar abundances to include two metal rich cases ($[\text{Fe}/\text{H}] = 0.5$ and 1.0) and an abundance pattern matching the observed peculiar ($\lambda\text{-boo}$ -type) subsolar abundances of HR8799 (Sadakane 2006). The best fitting model from this “evolution-consistent” grid has $T_{\text{eff}} = 896\text{K}$, $\log(g) = 4.3$, $[\text{Fe}/\text{H}] = 1.0$, $\log L_{\text{bol}}/L_{\odot} = -5.06$ (see Fig. 14). The agreement between this metal-rich model and the OSIRIS H and K -band spectra is similar to that of the previous hotter, solar abundance, best fit. The broad-band photometric comparison is also good (mostly to $1\text{-}\sigma$), but slightly worse compared to the solar abundance model at J and K bands (see Figure 14) but still consistent at $2\text{-}\sigma$. The lowering of T_{eff} by increasing metallicity is to be expected. Looking at the M_J versus $J - K$ CMD in Fig. 6, in order for cooler atmospheres to match HR8799b they need to be redder in $J - K$ and this can be accomplished by increasing metallicity and/or by decreasing the modal grain size (Burrows et al. 2006). The mean χ^2 for this metal-rich comparison is ~ 5.5 and only marginally better than the solar abundance model at the same temperature and gravity. However, given that even in this smaller grid the parameter space is still sparsely sampled, there is plenty of room for improvement.

6.2. Comparison to 2M1207 b

In near-IR CMDs, the object most similar to HR8799b is 2M1207b, a planet-mass companion to a young (~ 10 Myr) brown dwarf (Chauvin et al. 2005). In addition to their very red colors, these two objects also share the

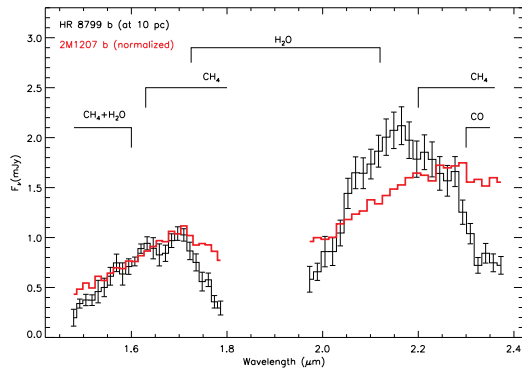


FIG. 15.— OSIRIS H and K -band spectra of HR8799b compared to the spectra of 2M1207b (Patience et al. 2010) binned to the same resolution and interpolated onto the same wavelength grid as the OSIRIS observations. The 2M1207b spectra were independently normalized for this comparison. The error-bars for the 2M1207b spectra are significantly smaller than those of HR8799b and, for clarity, are not shown.

same puzzling fact that their SEDs appear hotter than evolution models predict, for their ages and luminosities. Available photometry and spectroscopy of 2M1207b show all the signs of an object with effective temperature $\sim 1600\text{K}$ (Mohanty et al. 2007; Ducourant et al. 2008; Patience et al. 2010). When combined with current luminosity estimates ($\log(L/L_{\odot}) \sim -4.5$), the radius implied by this high effective temperature is $\sim 0.7 R_{\text{Jup}}$, comparable to the small size inferred above for HR8799b. Consequently, *both* 2M1207b and HR8799b are underluminous compared to hot-start evolution models and overluminous for cold start models, for their respective ages.

Mohanty et al. (2007) concluded that the high effective temperature was likely correct and, thus, 2M1207b is underluminous by ~ 2.5 magnitudes. Given that the distance to the source (52.4 ± 1.1 pc) is known (Ducourant et al. 2008), Mohanty et al. (2007) proposed that an edge-on disk surrounds 2M1207b providing the necessary extinction. Alternatively, Mamajek & Meyer (2007) proposed that 2M1207b is not a normal gas giant but rather the product of a recent protoplanetary collision and the observed flux is the afterglow from the hot, physically small, remnant. Given that HR8799b suffers from a similar quandary, it is unlikely that such rare events should be necessary to explain the first and only two objects found in the very red and faint regions of near-IR CMDs.

Given the puzzling similarities between 2M1207b and HR8799b mentioned above, it is useful to compare their SEDs. Moderate resolution ($R \sim 500 - 1500$) H and K -band spectra of 2M1207b (Patience et al. 2010) are compared to the HR8799b spectra in Figure 15. The spectrum of 2M1207b has shallower H_2O bands with a distinct CO band-head at $2.3 \mu\text{m}$ and no prominent CH_4 absorption – a spectrum very much like typical L dwarfs. The only feature the two sets of spectra have in common is a triangular shaped spectrum in the H band, consistent with both objects having low surface gravity (indicative of low mass and/or youth). Assuming both objects are not the result of recent protoplanetary collisions, 2M1207b and HR8799b may well represent important evolutionary states of substellar atmospheres. In-

dependent of the edge-on disk hypothesis, if the ages of the two systems are correct, then the planets’ masses are probably the same to within a factor of 2. If the masses are similar, then these objects provide evidence for rapid spectral changes from 10 to ~ 30 Myr for young planet-mass objects.

The analysis of HR8799b described above provides a third possible explanation for the properties of 2M1207b – namely that certain combinations of cloud coverage and non-equilibrium chemistry (and perhaps metallicity) are capable of producing a very low temperature object with an L-type near-IR spectrum. The two hypotheses proposed by Mohanty et al. and Mamajek et al. hinge on the assumption that the effective temperature of 2M1207b is $\sim 1600\text{K}$. However, looking back at Figure 6, 2M1207b is intersected by an intermediate cloudy model with $T_{\text{eff}} = 1100\text{K}$, close to evolution model predictions and consistent with a typical radius. Also, given the apparently extreme reduction of CH_4 in the atmosphere of HR8799b, it is conceivable that the CO/CH_4 mole fractions are quenched at even higher pressures in the younger (and likely lower gravity) atmosphere of 2M1207b, resulting in a low temperature atmosphere that is rich in CO (perhaps enough to produce a distinct CO bandhead at $2.3 \mu\text{m}$, as seen in the spectrum from Patience et al.) and without significant amounts of CH_4 . A search for such a cold, cloudy, model atmosphere with extreme non-equilibrium chemistry for 2M1207b is underway and will be presented in a separate paper (Barman et al., in prep.).

Despite their spectral differences, the most straightforward explanation for the positions of 2M1207b and HR8799b in near-IR CMDs is one of atmospheric origins. Instead of an edge-on disk or recent protoplanetary collision, a full exploration of the cloud properties, non-equilibrium chemistry, and metallicity is likely required to reproduce their observed SEDs with a model atmosphere having T_{eff} and $\log(g)$ consistent with evolution predictions. However, as more and more important physical processes are identified in substellar atmospheres, the number of free (and essentially independent) parameters increases and the ability to exhaustively explore all possible parameter combinations diminishes – more work (along the lines of Freytag et al. 2010) is clearly required to reduce the current set of parameters and produce more unified model atmospheres.

7. CONCLUSIONS

The HR8799 planetary system provides a rare opportunity to study multiple, coeval, giant planets at very young ages. The data and model comparisons described above are only first steps toward understanding just one of these planets and many challenging problems remain. While the data presented here offer the broadest spectral coverage for an HR8799 planet obtained so far, the low resolution and modest signal-to-noise set strong limits on what can be understood about HR8799b. In addition to the limits imposed by the data, the complexity and excess of free parameters in model atmospheres for giant planets and brown dwarfs also set strong limits on what can be confidently inferred from observations. With these limitations in mind, several conclusions can be drawn from the observations of HR8799b.

The SED of HR8799b is shaped by water absorp-

tion bands that are deeper than typically seen in late L and early T field dwarfs, but clearly consistent with a Hydrogen-rich planetary atmosphere. Only weak methane absorption is detected in the K band along with very weak CO absorption, indicating strong non-equilibrium chemistry and vertical mixing. Additional evidence for very weak methane absorption is seen in the H band spectrum (and narrow-band photometry). The near-IR spectra and broad-band photometry are smoothed and reddened by photospheric clouds not typical for brown dwarfs with $T_{\text{eff}} \leq 1100\text{K}$. The triangular shape of the H -band spectrum clearly indicates low surface gravity ($\log(g) < 5$), consistent with an age significantly younger than that proposed by Moya et al. (2010).

The best match from a solar abundance grid of model atmospheres (having $T_{\text{eff}} = 1100\text{K}$ and $\log(g) = 3.5$) found above implies a radius that is too small to be consistent with both the observed luminosity and the current understanding of the interiors and evolution of H+He-rich planets, regardless of mass, age, or interior core-size. Furthermore, a variety of model atmospheres can be constructed that fit the observed broad-band photometry very well (at least from the model grids used here), yet do not match the observed spectra – indicating that parameters inferred from broad-band photometric fits alone should be treated with caution.

While certainly not perfect, the model comparisons presented here are better representations of the observations than those presented by Bowler et al. (2010) and Currie et al. (2011). In particular, Bowler et al. found fits to their narrow-band spectrum that require $T_{\text{eff}} > 1100\text{K}$, which leads to unphysically small radii of $R < 0.75R_{\text{Jup}}$. These previous studies also had difficulty simultaneously fitting the photometry; for example, Currie et al. found it difficult to match most of the photometry, especially at $\lambda > 3\mu\text{m}$ (even with their thick or patchy cloud models) and Bowler et al. had difficulty matching the near-IR colors for reasonable T_{eff} . These difficulties may stem from the sparse sampling of model parameters in the grids used in these two studies (e.g. those parameters regulating non-eq. chemistry and clouds), though considerable degeneracies are present when fitting only broad-band photometry. Furthermore, the best fitting models for HR8799b found by Currie et al. typically have deeper methane absorption than seen in the broad K -band spectrum described above or the narrow-band spectrum of Bowler et al. Interestingly, Currie et al. emphasize cloud thickness/coverage over non-equilibrium chemistry, in particular as it pertains to the near-IR SED. The analysis presented here, however, requires deep quenching of CO/CH₄ to match the near-IR spectra (and near-IR narrow-band photometry), placing equal importance on both atmospheric effects when reproducing the observations.

Finding a solar abundance atmosphere that matches the complete set of data and interior/cooling-track predictions seems unlikely (though still not inconceivable). A more likely scenario is that the atmosphere of HR8799b has an elemental composition different from the Sun. A model atmosphere that matches the observations reasonably well (as well or better than any previous study), including the predictions of evolution models, can be found if the atmosphere is enhanced by a factor 10 in metals compared to the Sun. Such a model has $T_{\text{eff}} = 896\text{K}$ and

$\log(g) = 4.3$, consistent with a young giant planet with mass less than $10 M_{\text{Jup}}$. At ~ 30 Myrs, as recently proposed by Zuckerman et al. (2011), the mass of HR8799b would be 4 to $5 M_{\text{Jup}}$.

If HR8799b is indeed metal rich and near the very low end of the original mass range inferred by Marois et al. (2008), then core-accretion may be the preferred formation mechanism for the HR8799 planetary system. Metal enrichment, relative to the host star, is often considered a hallmark of the core-accretion scenario and recent work indicates that if the HR8799 planets formed by gravitation instabilities, they should show little metal enhancement (Helled & Bodenheimer 2010). Atmosphere models with either solar abundances or the metal poor λ -boo-like abundances of the star result in T_{eff} that are too high and corresponding radii that are too small. The analysis of Bowler et al. (2010) also indicates that enhanced metals (and low gravity) are likely to produce the best model fits.

While these conclusions rest heavily on models not tested by a large population of young giant planets (such a population should emerge in the coming years), the conclusions are self-supporting. Low surface gravity, clearly preferred by the model fitting (regardless of metallicity) and indicated by the shape of the H -band spectrum, may well allow for more efficient vertical mixing. As surface gravity decreases, the radiative-convection boundary moves closer to the photosphere, the maximum convective velocity increases, and K_{zz} also increases, at least in the convection zone (Freytag et al. 2010; Rice et al. 2011). Enhanced vertical mixing leads to enhanced non-equilibrium chemistry, as suggested by the absence of CH₄ absorption in both H and K bands. However, the connection between gravity and mixing is merely suggestive as the primary physical mechanism for mixing into the radiative zone unknown. Low surface gravity may also establish atmospheric conditions (not found in the higher gravity field T dwarfs) that support thick clouds at photospheric depths, allowing the intersection of the T-P curve and the condensation curve to be near the photosphere even at low T_{eff} . A connection between clouds and surface gravity is already starting to emerge for brown dwarfs. Evidence for a gravity dependence for the L-to-T transition has already been reported (Metchev & Hillenbrand 2006; Saumon & Marley 2008) and, recently, Stephens et al. (2009) found that low-gravity brown dwarfs in their sample remain cloudy at lower effective temperatures, with the L-to-T transition temperature decreasing from 1300K to 1100K as $\log(g)$ decreases from 5.0 to 4.5. Metchev & Hillenbrand (2006) also found that HD20303B, a low gravity transition brown dwarf, is $\sim 250\text{K}$ cooler than field objects with similar spectral types. If HR8799b has a $\log(g) \sim 4$, then it is possible that this emerging trend extends to this object as well, and would suggest that very low gravity objects (like young giant planets) are cloudy down to temperatures well below 1000K. The structure of the clouds needed to reproduce the colors and spectra of the HR8799 planets and 2m1207b are similar to those needed for late L-dwarfs. This suggests that such objects, from an atmospheric point of view, are extensions of the L-type field dwarfs rather than members of a new class altogether. This conclusion is distinct from that of Currie et al. who claim the clouds must be significantly

thicker than those required to match L dwarfs. Finally, enhanced metals would also lead to enhanced grain formation and conditions ripe for atmospheric cloud formation. The combination of these atmospheric conditions lead to bulk properties, inferred from the SED analysis alone, that include a radius consistent with the observed luminosity and current understanding of giant planet interiors, as well as a mass that fits comfortably within the limits required for long-term dynamical stability.

We thank the referee, Jonathan Fortney, for his careful review of our paper. Additional thanks go out to Shelley Wright, Jim Lyke, and James Larkin for their assistance with all things OSIRIS-related. We also thank Brad Hansen, Mark Marley, Didier Saumon, and Tristan Guillot for many useful discussions on the vagaries of planets and brown dwarfs. We are indebted to Jim Lyke, Al Conrad, Hien Tran, Scott Dahm, Randy Campbell, Terry Stickel and the entire Keck staff for their assistance in maximizing our observing efficiency. TB acknowledges the Kavli Institute for Theoretical Physics

and the participants of the 2010 workshop on Exoplanets for providing a stimulating environment. This research has benefited from the SpeX Prism Spectral Libraries, maintained by Adam Burgasser. The data presented herein were obtained at the W.M. Keck Observatory, which is operated as a scientific partnership among the California Institute of Technology, the University of California and the National Aeronautics and Space Administration. The Observatory was made possible by the generous financial support of the W.M. Keck Foundation. The authors wish to recognize and acknowledge the very significant cultural role and reverence that the summit of Mauna Kea has always had within the indigenous Hawaiian community. We are most fortunate to have the opportunity to conduct observations from this mountain. Most of the numerical work was carried out at the NASA Advanced Supercomputing facilities. This research was supported by NASA Origins of Solar Systems grants to LLNL and Lowell Observatory. This research was also supported by JPL/NexSci RSA awards. We thank all these institutions for their support.

REFERENCES

- Ackerman, A. S. & Marley, M. S. 2001, *ApJ*, 556, 872
 Allard, F., Allard, N. F., Homeier, D., Kielkopf, J., McCaughrean, M. J., & Spiegelman, F. 2007, *A&A*, 474, L21
 Allard, F., Hauschildt, P. H., Alexander, D. R., Tamanai, A., & Schweitzer, A. 2001, *ApJ*, 556, 357
 Asplund, M., Grevesse, N., & Sauval, A. J. 2005, in *Astronomical Society of the Pacific Conference Series*, Vol. 336, *Cosmic Abundances as Records of Stellar Evolution and Nucleosynthesis*, ed. T. G. Barnes III & F. N. Bash, 25–
 Baraffe, I., Chabrier, G., Allard, F., & Hauschildt, P. H. 2002, *A&A*, 382, 563
 Baraffe, I., Chabrier, G., & Barman, T. 2008, *A&A*, 482, 315
 Baraffe, I., Chabrier, G., Barman, T. S., Allard, F., & Hauschildt, P. H. 2003, *A&A*, 402, 701
 Barber, R. J., Tennyson, J., Harris, G. J., & Tolchenov, R. N. 2006, *VizieR Online Data Catalog*, 6119, 0
 Borysow, A., Jorgensen, U. G., & Zheng, C. 1997, *A&A*, 324, 185
 Bowler, B. P., Liu, M. C., Dupuy, T. J., & Cushing, M. C. 2010, *ArXiv e-prints*
 Burgasser, A. J., Burrows, A., & Kirkpatrick, J. D. 2006, *ApJ*, 639, 1095
 Burgasser, A. J., Cruz, K. L., Cushing, M., Gelino, C. R., Looper, D. L., Faherty, J. K., Kirkpatrick, J. D., & Reid, I. N. 2010, *ApJ*, 710, 1142
 Burgasser, A. J., Marley, M. S., Ackerman, A. S., Saumon, D., Lodders, K., Dahn, C. C., Harris, H. C., & Kirkpatrick, J. D. 2002, *ApJ*, 571, L151
 Burningham, B., Pinfield, D. J., Lucas, P. W., Leggett, S. K., Deacon, N. R., Tamura, M., Tinney, C. G., Lodieu, N., Zhang, Z. H., Huelamo, N., Jones, H. R. A., Murray, D. N., Mortlock, D. J., Patel, M., Barrado Y Navascués, D., Zapatero Osorio, M. R., Ishii, M., Kuzuhara, M., & Smart, R. L. 2010, *MNRAS*, 406, 1885
 Burrows, A., Sudarsky, D., & Hubeny, I. 2006, *ApJ*, 640, 1063
 Casewell, S. L., Dobbie, P. D., Hodgkin, S. T., Moraux, E., Jameson, R. F., Hambly, N. C., Irwin, J., & Lodieu, N. 2007, *MNRAS*, 378, 1131
 Chabrier, G., Baraffe, I., Allard, F., & Hauschildt, P. 2000, *ApJ*, 542, 464
 Chauvin, G., Lagrange, A., Dumas, C., Zuckerman, B., Mouillet, D., Song, I., Beuzit, J., & Lowrance, P. 2005, *A&A*, 438, L25
 Chiu, K., Fan, X., Leggett, S. K., Golimowski, D. A., Zheng, W., Geballe, T. R., Schneider, D. P., & Brinkmann, J. 2006, *AJ*, 131, 2722
 Cooper, C. S., Sudarsky, D., Milsom, J. A., Lunine, J. I., & Burrows, A. 2003, *ApJ*, 586, 1320
 Currie, T., Burrows, A. S., Itoh, Y., Matsumura, S., Fukagawa, M., Apai, D., Madhusudhan, N., Hinz, P. M., Rodigas, T., Kasper, M., Pyo, T., & Ogino, S. 2011, *ArXiv e-prints*
 Dodson-Robinson, S. E., Veras, D., Ford, E. B., & Beichman, C. A. 2009, *ApJ*, 707, 79
 Ducourant, C., Teixeira, R., Chauvin, G., Daigne, G., Le Campion, J., Song, I., & Zuckerman, B. 2008, *A&A*, 477, L1
 Dupuy, T. J., Liu, M. C., Bowler, B. P., Cushing, M. C., Helling, C., Witte, S., & Hauschildt, P. 2010, *ApJ*, 721, 1725
 Fabrycky, D. C. & Murray-Clay, R. A. 2010, *ApJ*, 710, 1408
 Faherty, J. K., Burgasser, A. J., Cruz, K. L., Shara, M. M., Walter, F. M., & Gelino, C. R. 2009, *AJ*, 137, 1
 Fegley, Jr., B. & Lodders, K. 1996, *ApJ*, 472, L37+
 Ferguson, J. W., Alexander, D. R., Allard, F., Barman, T., Bodnarik, J. G., Hauschildt, P. H., Heffner-Wong, A., & Tamanai, A. 2005, *ApJ*, 623, 585
 Fortney, J. J., Marley, M. S., Saumon, D., & Lodders, K. 2008, *ApJ*, 683, 1104
 Freytag, B., Allard, F., Ludwig, H., Homeier, D., & Steffen, M. 2010, *A&A*, 513, A19+
 Geballe, T. R., Saumon, D., Golimowski, D. A., Leggett, S. K., Marley, M. S., & Noll, K. S. 2009, *ApJ*, 695, 844
 Golimowski, D. A., Leggett, S. K., Marley, M. S., Fan, X., Geballe, T. R., Knapp, G. R., Vrba, F. J., Henden, A. A., Luginbuhl, C. B., Guetter, H. H., Munn, J. A., Canzian, B., Zheng, W., Tsvetanov, Z. I., Chiu, K., Glazebrook, K., Hoversten, E. A., Schneider, D. P., & Brinkmann, J. 2004, *AJ*, 127, 3516
 Goździewski, K. & Migaszewski, C. 2009, *MNRAS*, 397, L16
 Hauschildt, P. H., Baron, E., & Allard, F. 1997, *ApJ*, 483, 390
 Hauschildt, P. H., Warmbier, R., Schneider, R., & Barman, T. 2009, *A&A*, 504, 225
 Helled, R. & Bodenheimer, P. 2010, *Icarus*, 207, 503
 Helling, C., Ackerman, A., Allard, F., Dehn, M., Hauschildt, P., Homeier, D., Lodders, K., Marley, M., Rietmeijer, F., Tsuji, T., & Woitke, P. 2008a, *MNRAS*, 391, 1854
 Helling, C., Woitke, P., & Thi, W. 2008b, *A&A*, 485, 547
 Hinz, P. M., Rodigas, T. J., Kenworthy, M. A., Sivanandam, S., Heinze, A. N., Mamajek, E. E., & Meyer, M. R. 2010, *ApJ*, 716, 417
 Hubeny, I. & Burrows, A. 2007, *ApJ*, 669, 1248
 Kalas, P., Graham, J. R., Chiang, E., Fitzgerald, M. P., Clampin, M., Kite, E. S., Stapelfeldt, K., Marois, C., & Krist, J. 2008, *Science*, 322, 1345
 Kirkpatrick, J. D., Barman, T. S., Burgasser, A. J., McGovern, M. R., McLean, I. S., Tinney, C. G., & Lowrance, P. J. 2006, *ApJ*, 639, 1120
 Kirkpatrick, J. D., Cruz, K. L., Barman, T. S., Burgasser, A. J., Looper, D. L., Tinney, C. G., Gelino, C. R., Lowrance, P. J., Liebert, J., Carpenter, J. M., Hillenbrand, L. A., & Stauffer, J. R. 2008, *ApJ*, 689, 1295
 Knapp, G. R., Leggett, S. K., Fan, X., Marley, M. S., Geballe, T. R., Golimowski, D. A., Finkbeiner, D., Gunn, J. E., Hennawi, J., Ivezić, Z., Lupton, R. H., Schlegel, D. J., Strauss, M. A., Tsvetanov, Z. I., Chiu, K., Hoversten, E. A., Glazebrook, K., Zheng, W., Hendrickson, M., Williams, C. C., Uomoto, A., Vrba, F. J., Henden, A. A., Luginbuhl, C. B., Guetter, H. H., Munn, J. A., Canzian, B., Schneider, D. P., & Brinkmann, J. 2004, *AJ*, 127, 3553
 Konopacky, Q. M., Ghez, A. M., Barman, T. S., Rice, E. L., Bailey, J. I., White, R. J., McLean, I. S., & Duchêne, G. 2010, *ApJ*, 711, 1087

- Krabbe, A., Gasaway, T., Song, I., Iserlohe, C., Weiss, J., Larkin, J. E., Barczys, M., & Lafreniere, D. 2004, in *Society of Photo-Optical Instrumentation Engineers (SPIE) Conference Series*, Vol. 5492, *Society of Photo-Optical Instrumentation Engineers (SPIE) Conference Series*, ed. A. F. M. Moorwood & M. Iye, 1403–1410
- Lafrenière, D., Jayawardhana, R., & van Kerkwijk, M. H. 2008, *ApJ*, 689, L153
- Lafrenière, D., Marois, C., Doyon, R., & Barman, T. 2009, *ApJ*, 694, L148
- Lafrenière, D., Marois, C., Doyon, R., Nadeau, D., & Artigau, É. 2007, *ApJ*, 660, 770
- Lagrange, A.-M., Gratadour, D., Chauvin, G., Fusco, T., Ehrenreich, D., Mouillet, D., Rousset, G., Rouan, D., Allard, F., Gendron, É., Charton, J., Mugnier, L., Rabou, P., Montri, J., & Lacombe, F. 2009, *A&A*, 493, L21
- Larkin, J., Barczys, M., Krabbe, A., Adkins, S., Aliado, T., Amico, P., Brims, G., Campbell, R., Canfield, J., Gasaway, T., Honey, A., Iserlohe, C., Johnson, C., Kress, E., Lafreniere, D., Magnone, K., Magnone, N., McElwain, M., Moon, J., Quirrenbach, A., Skulason, G., Song, I., Spencer, M., Weiss, J., & Wright, S. 2006, *New Astron. Rev.*, 50, 362
- Leggett, S. K., Golimowski, D. A., Fan, X., Geballe, T. R., Knapp, G. R., Brinkmann, J., Csabai, I., Gunn, J. E., Hawley, S. L., Henry, T. J., Hindsley, R., Ivezić, Ž., Lupton, R. H., Pier, J. R., Schneider, D. P., Smith, J. A., Strauss, M. A., Uomoto, A., & York, D. G. 2002, *ApJ*, 564, 452
- Leggett, S. K., Saumon, D., Marley, M. S., Geballe, T. R., Golimowski, D. A., Stephens, D., & Fan, X. 2007, *ApJ*, 655, 1079
- Liu, M. C., Dupuy, T. J., & Ireland, M. J. 2008, *ApJ*, 689, 436
- Liu, M. C., Dupuy, T. J., & Leggett, S. K. 2010, *ApJ*, 722, 311
- Lodders, K. & Fegley, B. 2002, *Icarus*, 155, 393
- Lucas, P. W., Roche, P. F., Allard, F., & Hauschildt, P. H. 2001, *MNRAS*, 326, 695
- Mamajek, E. E. & Meyer, M. R. 2007, *ApJ*, 668, L175
- Marley, M. S., Fortney, J. J., Hubickyj, O., Bodenheimer, P., & Lissauer, J. J. 2007, *ApJ*, 655, 541
- Marley, M. S., Saumon, D., & Goldblatt, C. 2010, *ApJ*, 723, L117
- Marley, M. S., Seager, S., Saumon, D., Lodders, K., Ackerman, A. S., Freedman, R. S., & Fan, X. 2002, *ApJ*, 568, 335
- Marois, C., Lafrenière, D., Doyon, R., Macintosh, B., & Nadeau, D. 2006, *ApJ*, 641, 556
- Marois, C., Macintosh, B., Barman, T., Zuckerman, B., Song, I., Patience, J., Lafrenière, D., & Doyon, R. 2008, *Science*, 322, 1348
- Marois, C., Zuckerman, B., Konopacky, Q. M., Macintosh, B., & Barman, T. 2010, *ArXiv e-prints*
- McElwain, M. W., Metchev, S. A., Larkin, J. E., Barczys, M., Iserlohe, C., Krabbe, A., Quirrenbach, A., Weiss, J., & Wright, S. A. 2007, *ApJ*, 656, 505
- Metchev, S., Marois, C., & Zuckerman, B. 2009, *ApJ*, 705, L204
- Metchev, S. A. & Hillenbrand, L. A. 2006, *ApJ*, 651, 1166
- Mohanty, S., Jayawardhana, R., Huélamo, N., & Mamajek, E. 2007, *ApJ*, 657, 1064
- Moya, A., Amado, P. J., Barrado, D., García Hernández, A., Aberasturi, M., Montesinos, B., & Aceituno, F. 2010, *MNRAS*, 405, L81
- Noll, K. S., Geballe, T. R., & Marley, M. S. 1997, *ApJ*, 489, L87+
- Patience, J., King, R. R., de Rosa, R. J., & Marois, C. 2010, *A&A*, 517, A76+
- Patten, B. M., Stauffer, J. R., Burrows, A., Marengo, M., Hora, J. L., Luhman, K. L., Sonnett, S. M., Henry, T. J., Raghavan, D., Megeath, S. T., Liebert, J., & Fazio, G. G. 2006, *ApJ*, 651, 502
- Prinn, R. G. & Barshay, S. S. 1977, *Science*, 198, 1031
- Reid, I. N., Cruz, K. L., Kirkpatrick, J. D., Allen, P. R., Mungall, F., Liebert, J., Lowrance, P., & Sweet, A. 2008, *AJ*, 136, 1290
- Reidemeister, M., Krivov, A. V., Schmidt, T. O. B., Fiedler, S., Müller, S., Löhne, T., & Neuhäuser, R. 2009, *A&A*, 503, 247
- Rice, E. L., Faherty, J. K., Cruz, K., Barman, T.,Looper, D., Malo, L., Mamajek, E. E., Metchev, S., & Shkolnik, E. L. 2011, *ArXiv e-prints*
- Sadakane, K. 2006, *PASJ*, 58, 1023
- Saumon, D., Geballe, T. R., Leggett, S. K., Marley, M. S., Freedman, R. S., Lodders, K., Fegley, Jr., B., & Sengupta, S. K. 2000, *ApJ*, 541, 374
- Saumon, D. & Marley, M. S. 2008, *ApJ*, 689, 1327
- Saumon, D., Marley, M. S., Cushing, M. C., Leggett, S. K., Roellig, T. L., Lodders, K., & Freedman, R. S. 2006, *ApJ*, 647, 552
- Smith, M. D. 1998, *Icarus*, 132, 176
- Sparks, W. B. & Ford, H. C. 2002, *ApJ*, 578, 543
- Stephens, D. C., Leggett, S. K., Cushing, M. C., Marley, M. S., Saumon, D., Geballe, T. R., Golimowski, D. A., Fan, X., & Noll, K. S. 2009, *ApJ*, 702, 154
- Toomey, D. W. & Ftaclas, C. 2003, in *Society of Photo-Optical Instrumentation Engineers (SPIE) Conference Series*, Vol. 4841, *Society of Photo-Optical Instrumentation Engineers (SPIE) Conference Series*, ed. M. Iye & A. F. M. Moorwood, 889–900
- Tsuji, T. 2005, *ApJ*, 621, 1033
- van Leeuwen, F. 2007, *A&A*, 474, 653
- Visscher, C., Moses, J. I., & Saslow, S. A. 2010, *Icarus*, 209, 602
- Warmbier, R., Schneider, R., Sharma, A. R., Braams, B. J., Bowman, J. M., & Hauschildt, P. H. 2009, *A&A*, 495, 655
- Yung, Y. L., Drew, W. A., Pinto, J. P., & Friedl, R. R. 1988, *Icarus*, 73, 516
- Zuckerman, B., Rhee, J. H., Song, I., & Bessell, M. S. 2011, *ApJ*, in press